AGU PUBLICATIONS

Tectonics

RESEARCH ARTICLE
10.1002/2015TC003843

Key Points:
- Effects of erosion, sedimentation, and topography on fold linkage
- Effects of topography on the saddle point location and the reservoir closure
- Interaction between small-amplitude solution and erosion velocity

Correspondence to:
M. Collignon,
marine.collignon@erdw.ethz.ch

Citation:
Collignon, M., N. Fernandez, and B. J. P. Kaus (2015), Influence of surface processes and initial topography on lateral fold growth and fold linkage mode, *Tectonics*, *34*, doi:10.1002/2015TC003843.

Received 4 FEB 2015
Accepted 3 JUL 2015
Accepted article online 14 JUL 2015

Influence of surface processes and initial topography on lateral fold growth and fold linkage mode

M. Collignon[1], N. Fernandez[2,3], and B. J. P. Kaus[2]

[1]Geological Institute, ETH Zürich, Zürich, Switzerland, [2]Institute Geosciences, Johannes Gutenberg University, Mainz, Germany, [3]Now at Bureau of Economic Geology, Jackson School of Geosciences, University of Texas at Austin, Austin, Texas, USA

Abstract Elongation of randomly distributed fold segments and their potential linkage are important for hydrocarbon exploration because it can greatly influence the morphology of the reservoir and both migration and accumulation of hydrocarbons in antiformal traps. Here we study the effects of surface processes and the presence of a topographic slope on the different linkage modes that can occur, and how these parameters affect the required horizontal offset for perturbations to link. The proposed numerical model represents a sedimentary cover detached over a much weaker basal décollement layer. The upper surface is modified by mass redistribution, which is achieved by a combination of fluvial and hillslope processes. Several series of simulations were performed: (1) without surface processes or regional slope, (2) with regional slope only, (3) with fluvial incision and hillslope processes, and (4) with hillslope processes only. Model results show that the presence of a regional slope reduces the critical distance required for the transition between linkage and no linkage modes, whereas erosion and redeposition of sediments, on the contrary, increase this distance. The location of the saddle point, where fold segments link, and its vertical distance to the crests of the anticlines are different compared to the case without erosion or initial topographic slope, which potentially can affect the morphology of hydrocarbon traps. Moreover, both erosion and redeposition of sediments enhance the fold elongation (growth along the fold axis), once the erosion velocity exceeds the folding velocity. Model results have been compared to the Zagros Fold Belt.

1. Introduction

Many analogue [*Abbassi and Mancktelow*, 1992; *Cobbold*, 1975; *Mancktelow*, 2001], theoretical [*Biot*, 1961, 1965, 1966; *Fletcher*, 1991], and numerical [*Burg and Podladchikov*, 1999, 2000; *Schmalholz et al*., 2002; *Schmid and Podladchikov*, 2006] studies have investigated the mechanics of folding instability and fold growth for various rheologies, e.g., viscous and viscoelastic [*Biot*, 1961], viscous power law [*Fletcher*, 1974], and viscoelasto plastic [*Yamato et al*., 2011]. Despite notable analogue [*Ghosh and Ramberg*, 1968; *Grujic*, 1993; *Johns and Mosher*, 1996] and numerical [*Fletcher*, 1995; *Kaus and Schmalholz*, 2006; *Schmalholz*, 2008; *Schmid et al*., 2008] studies, many aspects of three-dimensional folding, such as fold elongation and fold linkage, are not fully understood. Fold linkage is important for hydrocarbon exploration, as it can greatly influence both migration and accumulation of hydrocarbons in antiformal traps [*Jolley et al*., 2007; *Sales*, 1997].

Landscape geomorphology provides an indirect observation of the tectonic activity. Surface processes and tectonics interact to create a wide variety of landscapes. Studies of the drainage network and quantitative geomorphic analyses can be used to understand the history of fault segments [*Delcailleau et al*., 2006; *Vergés*, 2007]. Asymmetry of the drainage network, lateral deflection of rivers, and/or the presence of one or several wind gaps can record amplification and elongation of embryonic fold segments [*Bretis et al*., 2011; *Keller et al*., 1999; *Ramsey et al*., 2008]. These fold segments would lengthen in the direction along fold axis and link together to form long folds. This mechanism has been suggested for the Zagros Fold Belt, both in the Fars Province [*Ramsey et al*., 2008] and in Kurdistan, NE Iraq [*Bretis et al*., 2011], where the axial lengths of single folds can reach more than 100 km. Following the theoretical model of *Bretis et al*. [2011], *Grasemann and Schmalholz* [2012] have numerically investigated the distance between two isolated elongating folds to explain four different modes of linkage: (1) linear linkage, (2) oblique linkage, (3) oblique no linkage, and (4) linear no linkage. However, the effects of surface processes on three-dimensional fold growth were not considered in their work.

Interactions between erosion, sedimentation, and mountain building have been extensively studied. In general, while syntectonic sedimentation appears to control the development of basins in the external parts

Table 1. Physical Properties of the Mechanical Model Layers

Layer	Description	Thickness (m)	Viscosity (Pa s)	Density (kg m^{-3})
2	Sticky air	2000	10^{17}	0
1	Overburden	1000	10^{22}	2700
0	Salt	2000	10^{19}	2200

of the fold-and-thrust belts [*Bonnet et al*., 2007; *Fillon et al*., 2013; *Simpson*, 2006], erosion strongly influences the hinterland evolution by enhancing crustal uplift and exhumation of rocks [e.g., *Beaumont et al*., 1992; *Burbank*, 2002; *Kaus et al*., 2008; *Molnar and England*, 1990; *Montgomery and Brandon*, 2002]. Although most studies focused on brittle deformation, a few analogue and numerical studies tackled ductile deformation (e.g., folds), either at the scale of the fold [*Contreras*, 2010; *Nalpas et al*., 1999, 2003; *Pichot and Nalpas*, 2009; *Simpson*, 2004a] or at the scale of fold-and-thrust belt [*Simpson*, 2004b, 2004c]. Sedimentation may influence the shape and growth of folds, while erosion tends to intensify the fold growth rate. Erosion may localize deformation, leading to an important change in the folding pattern [*Simpson*, 2004a]. Our recent numerical multilayer folding experiments [*Collignon et al*., 2014], in which an initial random perturbation was prescribed, demonstrated that under efficient drainage network conditions, or when a nonzero initial topographic slope was applied to the model, the type of fold linkage could be modified.

Here we systematically investigate the effects of erosion and sedimentation on linkage modes and how it affects the maximal horizontal distance between two linking perturbations. For this purpose, we used a coupled 3-D mechanical and surface process model as in *Collignon et al*. [2014].

2. Numerical Model

We used the 3-D thermomechanical code Lithosphere and Mantle Evolution Model (LaMEM) [*Kaus et al*., 2012; *Popov and Kaus*, 2013], coupled to a landscape evolution model (both erosion and sedimentation). LaMEM solves the equations describing the conservation of momentum and mass for highly viscous incompressible fluids in three dimensions, using a staggered grid finite difference scheme. The landscape evolution model uses a nonlinear diffusion formulation, taking into account both fluvial and hillslope processes. The diffusion equation is discretized using the Galerkin finite element method [*Zienkiewicz and Taylor*, 2000] with bilinear shape and weighting functions using four-node quadrilateral elements. A description of both mechanical and surface process models (SPMs), as well as the manner in which they are coupled, can be found in *Collignon et al*. [2014]. Both models are only briefly described here, and the governing equations are listed in the appendices. In this study, we focus on the effects of surface processes on fold linkage and not on the deformation style (i.e., faulting versus folding). We consider conditions where the deformation is only accommodated by folding. For this reason and for computational efficiency, we use linear viscous constitutive laws. Furthermore, *Grasemann and Schmalholz* [2012] employed both linear and nonlinear viscosities and showed that they give similar linkage modes.

The $20 \times 40 \times 5$ km model consists of a thin stiff layer, resting on a weak décollement. The initial thickness ratio of the stiff to weak layer is 0.5, and the viscosity ratio is 1000 (Table 1). We used this viscosity ratio in order to obtain wavelengths corresponding to crustal-scale folds (i.e., on the order of 10 km), as well as for computational time reasons. Indeed, high-viscosity ratios allow a more rapid development of folds. The resulting modeled wavelengths are in the range of those reported for the Zagros Fold Belt [*Mouthereau et al*., 2007]. To localize folding at the desired location, we prescribe two geometrical step-like perturbations at the salt-sediment interface with a length and width of 1 and 2 km, respectively, and a height of 100 m (see Figure 1 and Table 2). These perturbations have the same viscosity as the décollement layer. The perturbations are located at two opposite sides of the model: Perturbation 1 (P1) is fixed in the middle of the *y* axis, whereas the other perturbation (P2) varied along the *y* axis, with a prescribed offset *D* (see Figure 1). There is a "sticky-air" layer above the two mechanical layers. The sticky air is used in combination with an internal free surface to approximate a true free surface [*Crameri et al*., 2012]. A regional slope β is defined at the interface between the sedimentary cover and the sticky air. This is required for the SPM to generate a drainage network. If no slope is prescribed, the drainage network can only develop after folding occurred and is not able to affect deformation [see *Simpson*, 2004c]. We impose zero shear stress (e.g., $\sigma_{ij}t_j = 0$, where t_j

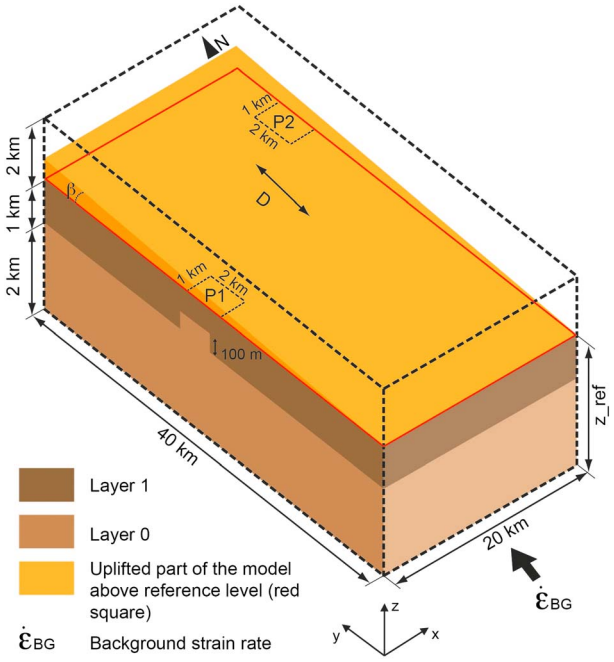

Figure 1. Schematic geometry (not to scale) of the model used in this study. A strong layer 1 lays on weak layer 0 (parameters in Table 2). The top layer is sticky air. Red plane: reference level (*z*_ref) with which the topography $h(x,y) = z\_\text{model} - z\_\text{ref}$ is defined. For visualization purposes, the *z* axis has been exaggerated.

is a unit vector tangent to the boundary) on all boundaries. A Dirichlet boundary condition is applied in the *y* direction as $V_y = \dot{\varepsilon}_{BG} y$, with $\dot{\varepsilon}_{BG} = -10^{14} s^{-1}$ being the background strain rate and V_y the velocity in the *y* direction; the *x* and lower boundaries have zero normal velocities, and the vertical velocity at the top boundary is proportional to the horizontal velocity such that mass in the model is conserved. The mechanical model used a resolution of $30 \times 60 \times 20$ elements. The marker resolution is of $4 \times 4 \times 8$ particles per cell in *x*, *y*, and *z* directions, respectively. The amplitude of the perturbation is 100 m (10% of the overburden thickness), which is close to *Grasemann and Schmalholz* [2012], whose perturbation amplitude represents 6.67% of their overburden. Due to the different numerical methods employed between this study (finite difference method) and the one of Grasemann and Schmalholz (finite element method), the perturbation amplitude in our model needs to be higher for similar numerical resolution, to resolve the perturbation and to ensure folding localization. Although the perturbation amplitude (100 m) is smaller than the vertical resolution of our model (250 m), the perturbation is still resolved as the marker resolution is sufficient (eight markers for 250 m), even when a regional slope is prescribed. The thickness ratios of perturbation

Table 2. Parameters Used in This Study

Symbol	Unit	Definition
Lx, *Ly*, *Lz*	m	Initial dimensions of the model in *x*, *y*, and *z*
x, *y*, *z*	m	Coordinates
*z*_ref	m	Reference level
H	m	Maximum initial elevation
h_0	m	Initial roughness of the surface processes model
c	$(m^2 s^{-1})^{1-n}$	Fluvial incision
k	$(m^2 s^{-1})$	Hillslope diffusion
n	-	Exponent for dependency of sediment transport on fluid discharge
α	$m s^{-1}$	Annual rainfall
q	$m^2 s^{-1}$	Surface fluid discharge
β	%	Regional slope (defined by *H*/*Ly**100)
η	Pa s	Viscosity
g	$m s^{-2}$	Gravity
δ	$kg m^{-3}$	Density
ε_{BG}	s^{-1}	Background strain rate (in *y* direction)
P1,P2	-	Initially prescribed perturbations
D	m	Initial distances between the prescribed perturbations
A_{max}	m	Maximum amplitude
A_{mid}	m	Amplitude in the middle of the prescribed perturbations
L	m	Low limb-dip wavelength developing in the numerical simulation
Δ_H	m	Difference in elevation between the saddle point and the crest of the anticline
S	%	Shortening
t	Ma	Time

Table 3. Summary of the Simulations[a]

Slope (%)	Hillslope Diffusion (k)	Fluvial Incision (c)	Offset (D)	Linkage	Locking	No Linkage
0	10^{-31}	0	7.5	X		
0	10^{-31}	0	8		X	
0	10^{-31}	0	8.5			X
0.125	10^{-31}	0	7.5	X		
0.125	10^{-31}	0	8		X	
0.125	10^{-31}	0	8.5			X
0.5	10^{-31}	0	7.5		X	
0.5	10^{-31}	0	8			X
0.5	10^{-31}	0	8.5			X
0.75	10^{-31}	0	7.5			X
0.75	10^{-31}	0	8			X
0.75	10^{-31}	0	8.5			X
0.5	10^{-11}	10	7.5		X	
0.5	10^{-11}	10	8			X
0.5	10^{-11}	10	8.5			X
0.5	10^{-11}	50	7.5	X		
0.5	10^{-11}	50	8			X
0.5	10^{-11}	50	8.5			X
0.5	10^{-11}	100	7.5	X		
0.5	10^{-11}	100	8			X
0.5	10^{-11}	100	8.5			X
0.5	4×10^{-7}	0	8	X		
0.5	8×10^{-7}	0	8	X		

[a]The cross (X) specifies which linkage mode is obtained: Linkage, locking, no linkage.

to overburden are, however, modified when a nonzero initial topographic slope is prescribed to the model, leading to different growth rate: higher thickness ratios result in higher fold growth rates [*Collignon et al.*, 2014]. For the SPM, the boundaries normal to the direction of compression are defined as base levels and are kept at constant elevation during a tectonic time step. Zero flux is prescribed on the other boundaries. The topography is updated after every mechanical time step, implying that the base level is only kept at constant elevation between two mechanical time steps while the SPM is run. The resolution of the SPM mesh is 5 times higher than the one used for the tectonic model (i.e., 150×300 elements). A previous study has shown that using resolution factors lower or equal to 10 did not influence the results [*Collignon et al.*, 2014]. To initiate river incision, we prescribe a random noise of 1 m amplitude at the topography surface. The same random noise was employed in all the simulations. Physical parameters used in this study are summarized in Table 2.

3. Results

A series of simulations were performed with different erosional intensities, by varying the regional slope, the fluvial incision, and/or the hillslope diffusion (see Table 3 for a summary of all simulations). For each simulation, only one parameter was modified to better understand the relative influence of the regional slope, the fluvial incision, or the hillslope processes. In the next remaining part of this paper, upper ($y=Ly$), lower ($y=0$), right ($x=Lx$), and left ($x=0$) parts of the model surface will be referred as north, south, east, and west, according to the north arrow used in figures. We will refer to the fold segments that developed above the initial prescribed perturbations P1 and P2 as F1 and F2, respectively. In our study, we mainly refer to the antiformal structure of the fold. Terminology used in the literature to describe 3-D fold growth can be misleading [*Frehner*, 2014, and references therein], especially for the two horizontal growth directions. We employ in this study the following terminology:

1. *Fold amplification* (z axis) is for the vertical growth.
2. *Fold elongation* (x axis) is for the growth along the fold axis.
3. *Sequential fold growth* (y axis) is for the growth in the shortening direction. It describes the growth of additional fold segments adjacent to the initial isolated fold.

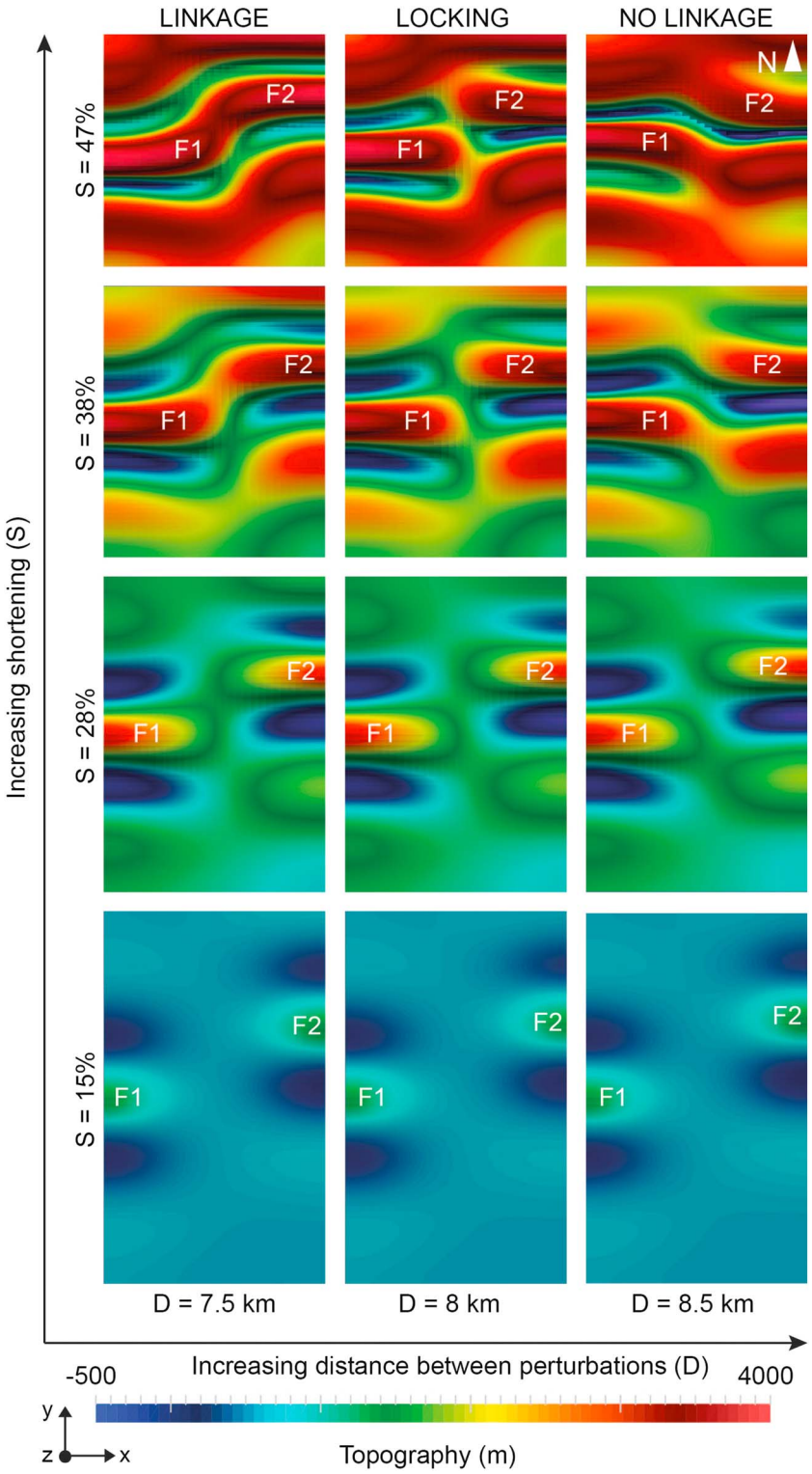

Figure 2. Evolution through increasing bulk shortening for three simulations with three distances between perturbations P1 and P2. Each simulation illustrates one of the linkage modes: linkage, locking, and no linkage. No surface processes or initial topography were considered.

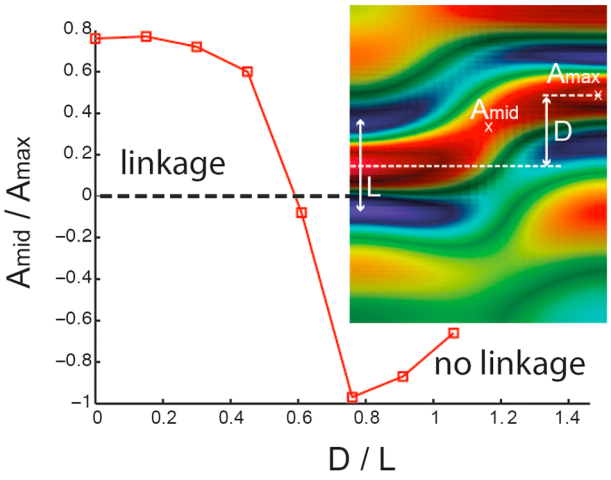

Figure 3. Ratio of A_{mid}/A_{max} versus D/L obtained in simulations with linear viscous materials (after a bulk shortening of 38%). Change in sign of A_{mid}/A_{max} indicates transition from linkage to no linkage and occurs for values of D/L between 0.6 and 0.8. The surface explains where A_{mid} and A_{max} are measured and how D and L were considered.

The sequential growth reflects the development of the full folding structure (development of several fold segments) that results from the three-dimensional growth of an instability and is not restricted to a single fold segment. Fold amplification and fold elongation are usually used to describe the growth of a single fold segment.

3.1. Linkage in the Absence of Surface Processes

To understand how erosion and sedimentation affect fold linkage, we first need to know for which initial distances or offsets, D, between two perturbations fold segments link (or not) in the absence of erosion and sedimentation (Figures 2 and A1). The critical distance, D_{crit}, corresponds to the minimal offset D above which fold segments no longer link. In a first set of simulations, we investigated different values for D: every 2 km from 0 to 14 km and every 500 m between 7 and 9 km, as 8 km appears to be the critical distance, D_{crit}. For this value ($D_{crit} = 8$ km), the fold segments F1 and F2 are locked by the sequential growth of the perturbations and the growth of adjacent fold segments. Folds are considered locked when they do not elongate anymore due to the interactions with other segments. Elongation of F1 and F2 is stopped, and they do not link with other fold segments. The locking case may resemble a triple linkage, where three fold segments link together at a single point, in a fork-shaped-like pattern, for less than 40% of bulk shortening (Figure 2). However, F1 and F2 will not link with any fold segments with increasing shortening in the case of locking. Instead, fold segments in north and south of the model respectively link and prevent the elongation of F1 and F2. F1 and F2 link when $D < D_{crit}$, while they do not link for $D > D_{crit}$. Instead, F1 links with another fold segment that forms to the south of F2 by sequential growth of the perturbation P2. Similarly, F2 links with a fold segment that forms to the north of F1 by sequential growth of the perturbation P1. The horizontal distance (y direction) between F1 (or F2) and the segment south of F2 (or north of F1) is smaller than the horizontal prescribed offset D between F1 and F2. Consequently, F1 and F2 will link with these adjacent segments rather than together. The measured wavelength of F1 and F2 is ~13.2 km. A critical value of 8 km for the locking case is obtained for the setup employed in this study. However, changing the viscosity contrast between layers and the background strain rate will modify fold growth rates and wavelengths of the perturbations and thus the value of the critical distance between linkage and no linkage modes. Two dimensionless ratios (Figure 3) are introduced to define the transition from linkage to no linkage modes [*Grasemann and Schmalholz*, 2012]. The first is the ratio of the initial distance, D, to the low limb-dip wavelength developing in the numerical simulation, L (Figure 3). The second is the ratio of the amplitude of the symmetric point between both perturbations (A_{mid}) and the maximum amplitude (A_{max}). The transition from linkage to no linkage occurs when the ratio A_{mid}/A_{max} changes sign and when the ratio D/L is close to 0.6 (Figure 3). This is valid for the case where no surface processes or initial topographic slope were applied to the model. As soon as surface processes are present, the maximum elevated areas are eroded and sediments are redistributed, resulting in a higher saddle point (and positive A_{mid} coordinates) than in the case without surface processes. The distinction between linkage and no linkage was done, by considering both the surface topography and surface folding velocities.

3.2. Influence of an Initial Topographic Slope on Fold Linkage

A second series of simulations was performed to investigate the influence of a regional slope β on the fold linkage. We considered D values every 500 m between 7 and 9 km. Fluvial incision was set to zero ($c = 0$)

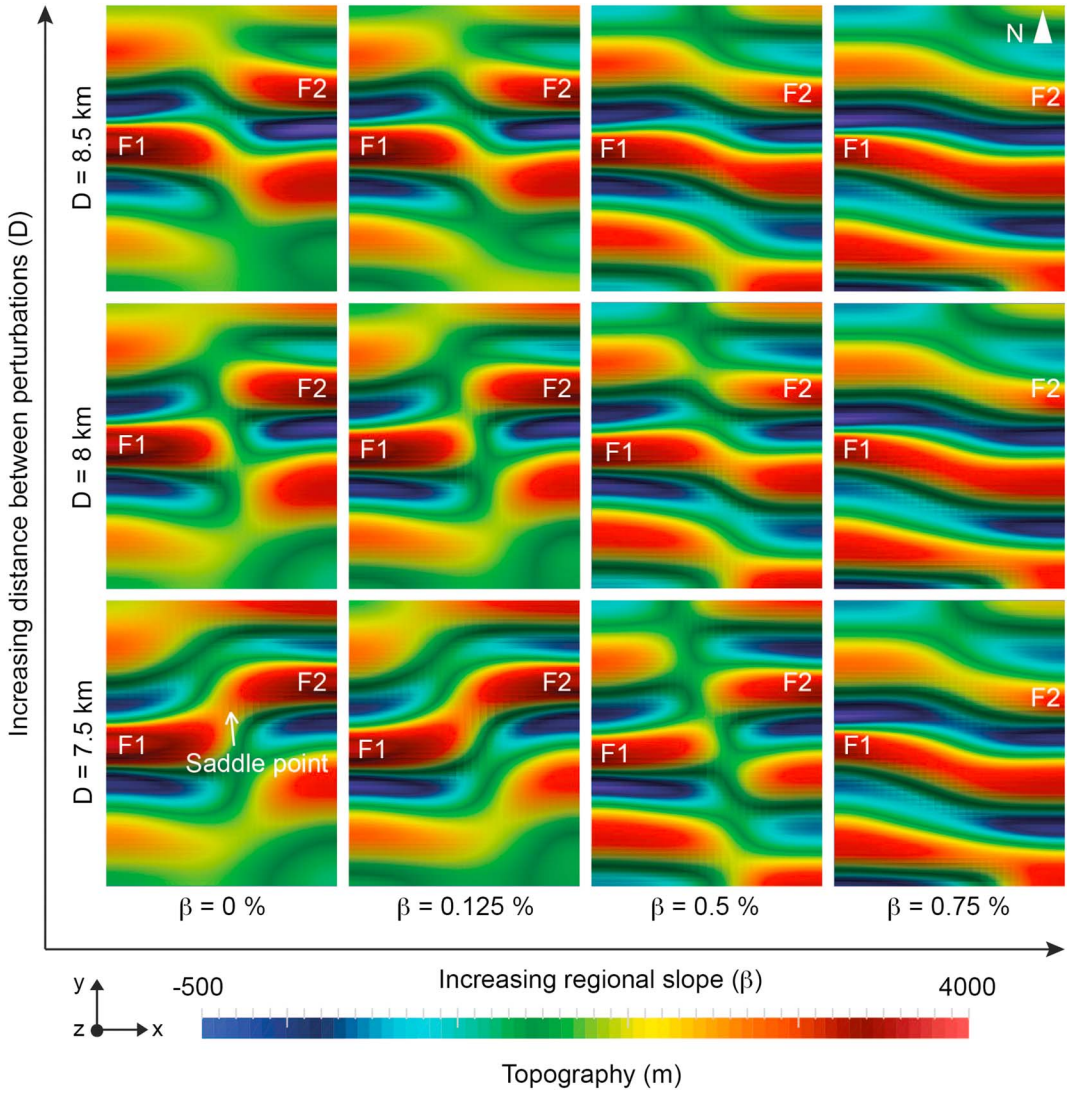

Figure 4. Model surface topographies after ca. 1.5 Ma and 38% shortening for different regional slopes (0, 0.125, 0.5, and 0.75%) and distances, *D* (7.5, 8.0, and 8.5 km), between two initial perturbations.

and the hillslope diffusion to a low value ($k = 10^{-31}\,m^2\,s^{-1}$), essentially eliminating erosion and sedimentation. Increasing the regional slope tends to reduce the critical distance, D_{crit} (Figure 4). For example, fold segments F1 and F2 link for $D = 7.5$ km and $\beta \leq 0.125\%$. The fold pattern resembles a triple linkage when the prescribed slope is 0.5%, and it is unclear whether F1 will link with F2, the fold segment that developed south of F2, or both when increasing shortening (Figure 4). F1 may also not link with any segments, leading to a locking case. Fold segments F1 and F2 do not link for higher regional slope ($\beta = 0.75\%$). They instead link with the fold segments that developed during the sequential growth of P1 and P2. The resulting long folds show a higher degree of cylindricity. When there is no regional slope, perturbations P1 and P2 amplify and grow similarly in all directions (*x*,*y*,*z*). After a bulk shortening of 38% (Figure 4), F1 and F2 correspond to the same maximum topographic elevation. F1 still corresponds to the maximum topographic elevation with increased regional slopes, while F2 is at lower elevation than F1 or some fold segments that developed in the southern part of the model. According to the topographic elevation in Figure 4, fold segments in the southern part of the model domain grow faster than in the northern part when a regional slope is prescribed.

Moreover, the coordinates (*x*,*y*,*z*) of the saddle point, where two fold segments link, are lower for higher regional slope β. The saddle point is then shifted to the southwestern part of the model (Figure 5). The difference in elevation between the saddle point and F1 (or F2) fold crest, Δ_H, generally tends to be higher with increased

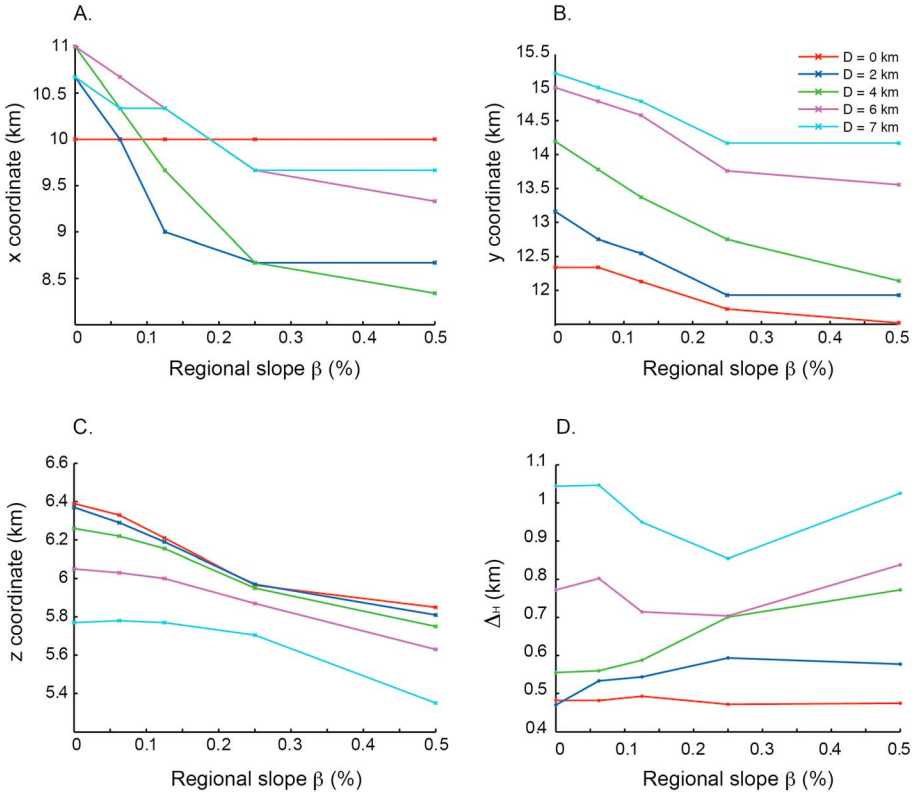

Figure 5. (a–c) Evolution, with increasing regional slope, of the coordinates of the saddle point for offsets $D = 0$, 2, 4, 6, and 7 km between perturbations P1 and P2. (d) Evolution, with increasing regional slope, of the difference in elevation between the saddle point and the fold crest.

regional slope β and offset D. Specifically, Δ_H remains at low values and does not show much variation with increased β when $D = 0$ (linear linkage). Δ_H increases with β for any values of D smaller than 5 km. Δ_H decreases when $D > 5$ km and $\beta \leq 0.25\%$ and increases when $D > 5$ km and $\beta > 0.25\%$ (Figure 5).

3.3. Influence of Erosion and Sedimentation on Fold Linkage

In the next series of simulations, we study the effects of erosion and redeposition of sediments on fold linkage. We first considered the effects of both fluvial incision and hillslope diffusion (Figure 6). For this purpose, we employed the SPM previously described (nonlinear diffusion law). We then investigate only the effects of hillslope processes, using a simple linear diffusion law [*Culling*, 1960]. As in previous simulations, we investigated the different cases with $D = 7.5$, 8, and 8.5 km, focusing now on a regional slope of $\beta = 0.5\%$ (Figure 6). This slope value allows the quick development of an incising drainage network, which has the possibility to affect the fold pattern [*Simpson*, 2004c]. Without erosion and sedimentation ($c = 0$ and $k = 10^{-31}\,m^2\,s^{-1}$), F1 and F2 do not link when $D \geq 8$ km and $\beta = 0.5\%$. Instead, F1 links with a fold segment south of F2, and similarly, F2 links with a fold segment north of F1, which formed during sequential growth of perturbations P1 and P2. Elongation of F1 and F2 seems impeded when $D = 7.5$ km and $\beta = 0.5\%$. At this stage, it is unclear whether F1 will link with F2, the fold segment south of F2 or both when increasing time and shortening. F1 and F2 may as well be locked with increased time and shortening. We here aim to find which linkage mode (no linkage, linkage, or locking) is favored by erosion and sedimentation.

The critical distance D_{crit} increases with increased erosion and sedimentation, independently from the SPM (nonlinear or linear diffusion) used in this study. F1 and F2 are able to link for larger initial offsets D than when no erosion and sedimentation are considered. Results obtained with both SPM are described next.

3.3.1. Fluvial Erosion (Nonlinear Diffusion)

Hillslope diffusivity (k) is set to $10^{-11}\,m^2\,s^{-1}$ for $c > 0$ and to $10^{-31}\,m^2\,s^{-1}$ for $c = 0$. Fluvial incision has the capacity to affect the fold pattern for values of D up to 8 km only. As an example, F1 and F2 now link

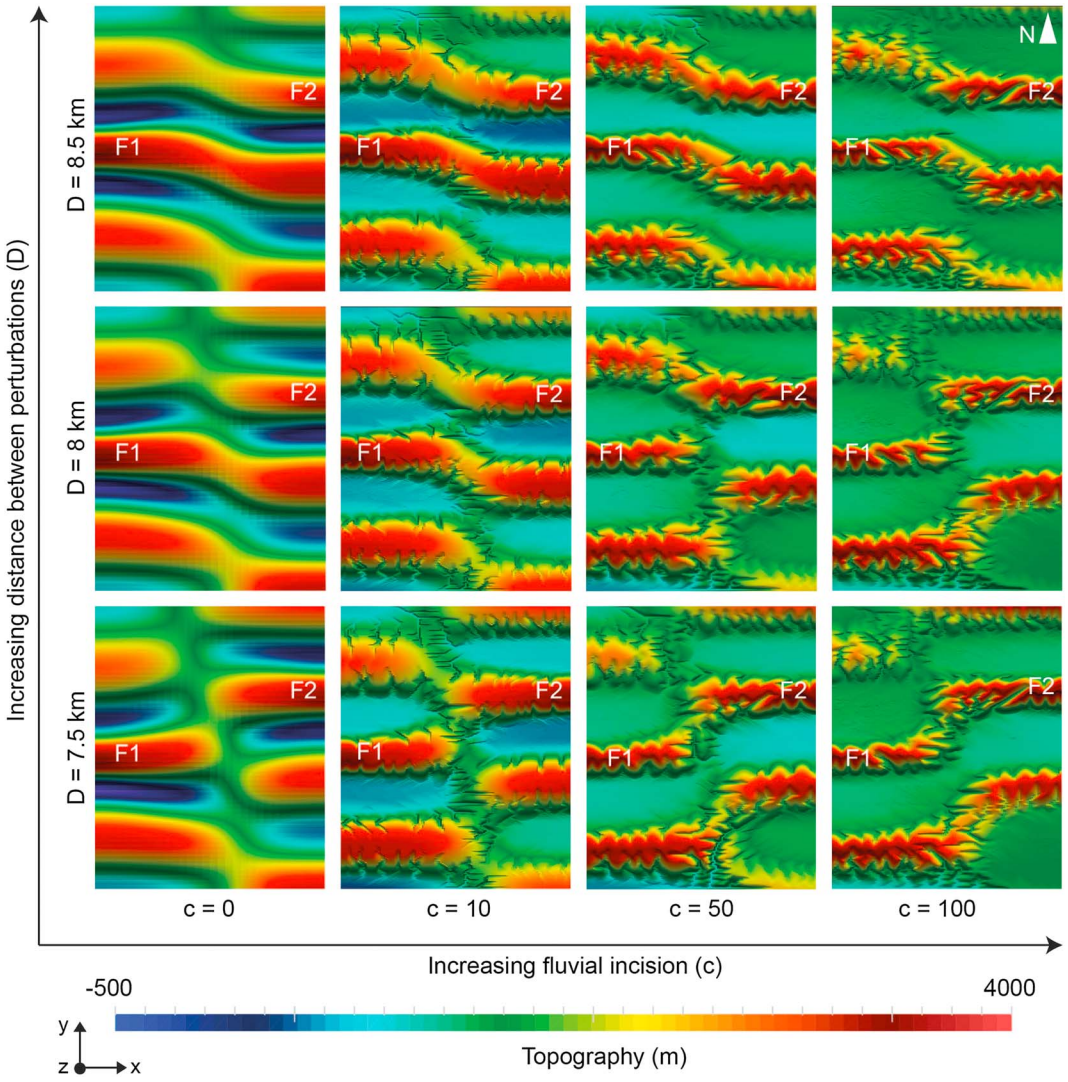

Figure 6. Model surface topography after ca. 1.5 Ma and 38% shortening for fluvial incision coefficients $c = 0$, 10, 50, and 100 and offsets $D = 7.5$, 8, and 8.5 km between two initial perturbations P1 and P2. Regional slope $\beta = 0.5\%$.

(Figure 6) for $D = 7.5$ km and high fluvial incision ($c \geq 50$). We observe a progressive transition with increasing fluvial incision from the case, which resembles a triple linkage and where it is not obvious if F1 will link with F2, the fold segment south of F2, or both, to a case where F1 and F2 truly link. Fold segments become more and more disconnected with increasing fluvial incision and their linkage is different (Figure 6). The fold segment south of F1 links with the one south of F2. In the case without erosion and sedimentation, the fold segment south of F1 links with the lowermost right (southeast) fold segment, developing at the lower boundary. Under high erosion, this latter fold segment does not topographically express. The fold pattern resembles a triple linkage when $D = 8$ km and $c = 100$, and it is unsure if F2 will link with F1, the fold segment north of F1 or both.

The temporal evolution of both the topography and the folding velocity is shown in Figure 7 for the case without and with erosion and for $D = 8$ km. The folding velocity corresponds to amplification of the initial perturbation at the salt-sediment interface and was differentiated from the uplift associated with thickening during compression. Folding velocity was computed using the vertical velocity (total uplift) obtained in the numerical model, from which the kinematic velocity (pure shear thickening), associated with the background strain rate, was extracted:

$$V_{z_{\text{folding}}} = V_{z_{\text{surface}}} * V_{\text{char}} - Z_{\text{surface}} * \dot{\varepsilon}_{\text{BG}}, \quad (1)$$

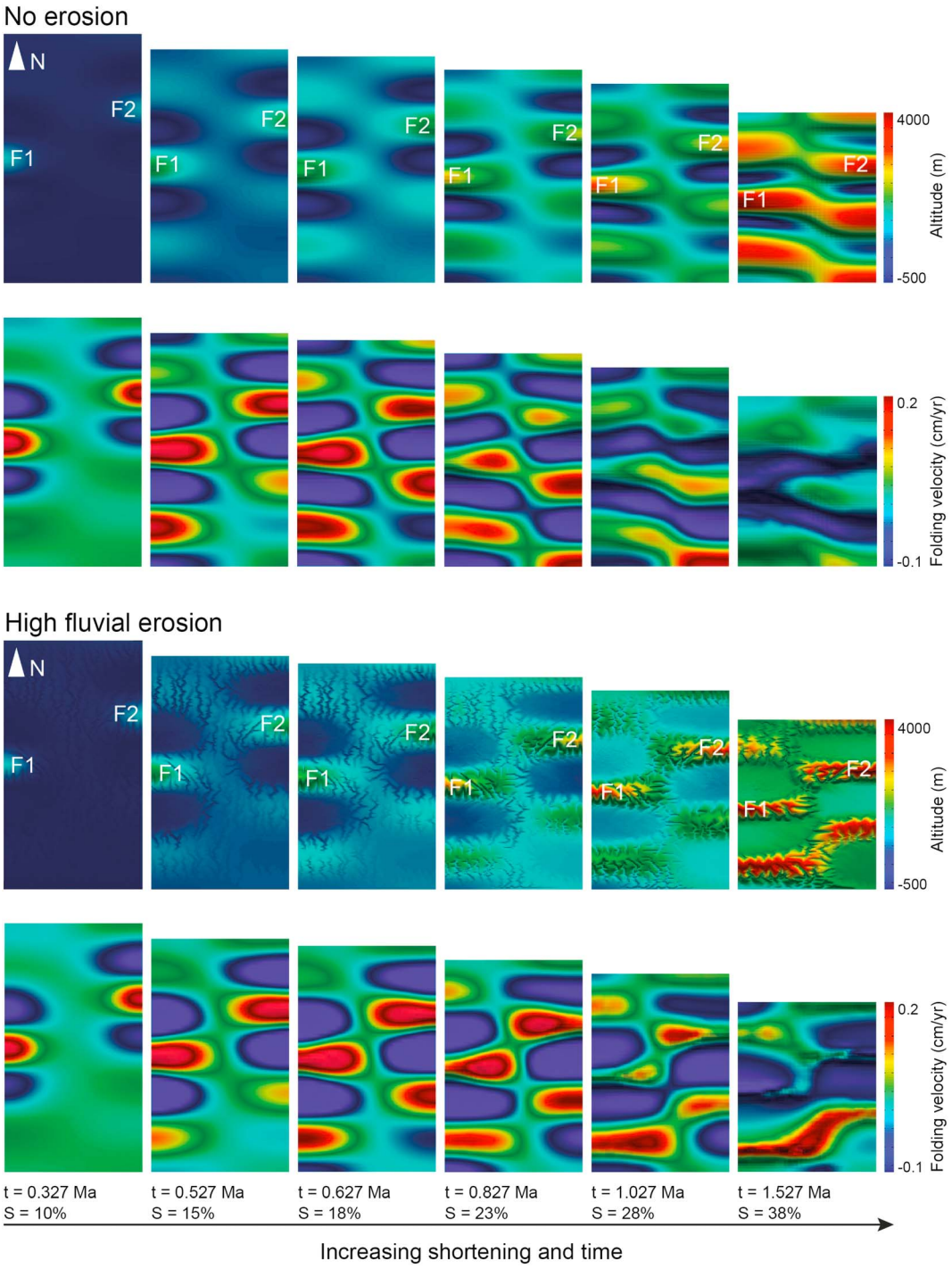

Figure 7. Evolution of the topography and folding velocity with increasing time and shortening for cases without erosion ($c = 0$, $k = 10^{-31}$ m^2 s^{-1}) and with high fluvial erosion ($c = 100$, $k = 10^{-11}$ m^2 s^{-1}). Initial regional slope $\beta = 0.5$ % and initial distance $D = 8$ km.

where $V_{z_{folding}}$ is the folding velocity, $V_{z_{surface}}$ the vertical velocity in non-dimensional units, $Z_{surface}$ the coordinates of the surface, $\dot{\varepsilon}_{BG}$ the background strain rate, and V_{char} the characteristic velocity. In simulations with erosion, one can expect the folding velocity to be affected by fluvial incision, as the model considers a feedback between mechanics and surface processes. Both topography and folding velocity patterns show some variations between cases with and without erosion. However, these variations become visible only after 18% shortening

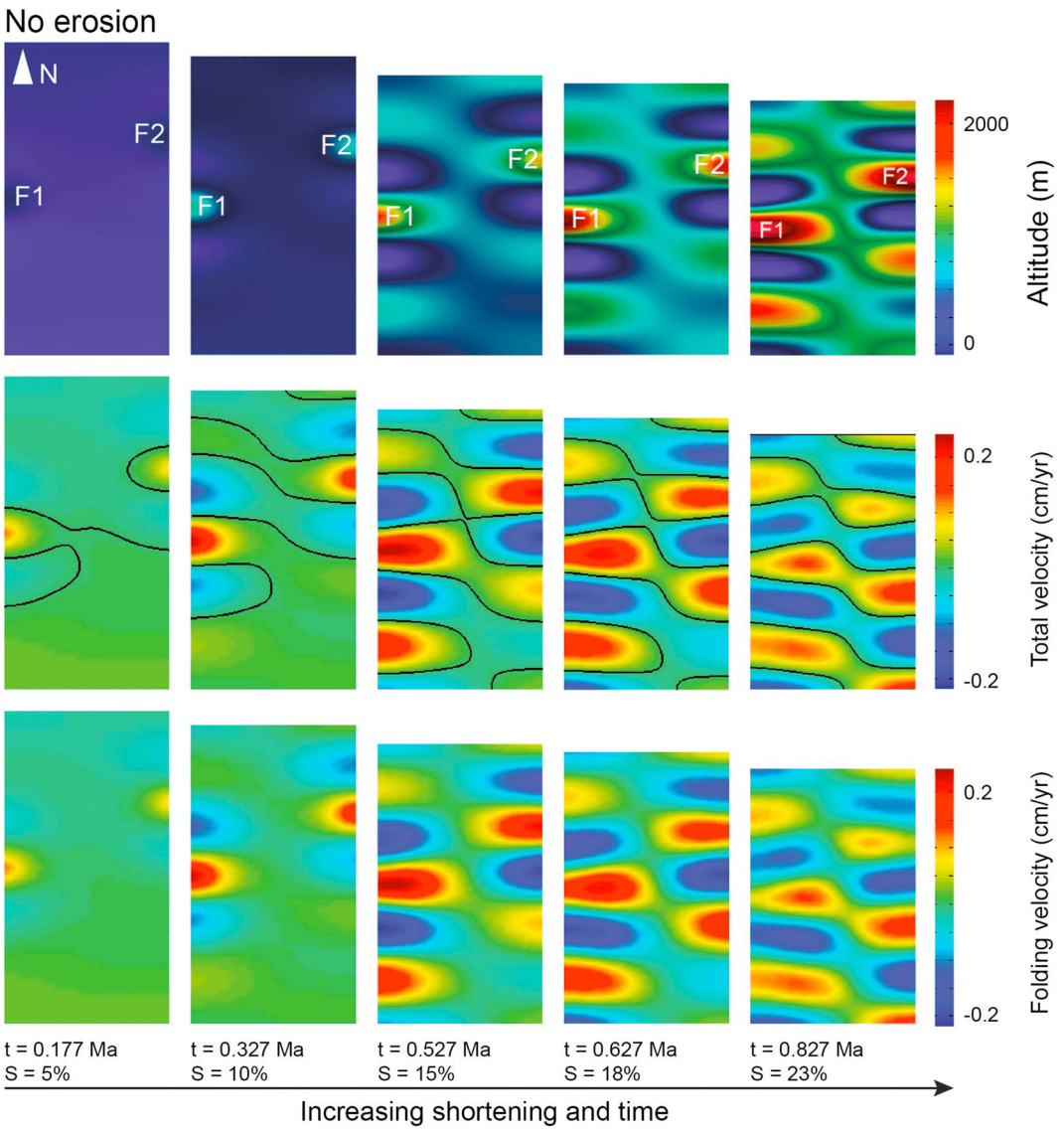

Figure 8. Time evolution of the topography and velocities for a case without erosion ($c = 0$, $k = 10^{-31}$ m^2 s^{-1}). Total velocity = sum of the folding and erosion velocities. The black contour line at 0. Initial regional slope $\beta = 0.5$ % and initial distance $D = 8$ km.

and 0.63 Ma (Figure 7). The variations in the topographic folding pattern for both simulations have been described above. The evolution of the folding velocity pattern (looking at the maximum velocity) shows that in cases both with and without erosion, fold segments F1 and F2 initially developed above P1 and P2, after which new fold segments formed adjacent to F1 and F2 (in the direction of shortening), as a result of sequential growth of the perturbations P1 and P2. The maximum velocity shifts from F1 and F2 to the adjacent fold segments, principally to the one located in the southern parts of the model, due to the presence of a thinner overburden. The folding velocity globally decreases with increased time and shortening when no fluvial incision is considered. At the end of the simulation, the maximum velocity in the case without fluvial incision is located at the lowermost right (southeast) fold segment, due to boundary conditions (the strain rate is applied at this boundary). The maximum folding velocity is reached at approximately 18% shortening and 0.63 Ma.

The maximum folding velocity is reached later, at approximately 23% and 0.83 Ma when fluvial erosion is present (Figure 7). In this case, the maximum folding velocity remains longer at the locations of F1 and F2, before being shifted to the lowermost left fold segment (southwest). This may explain why the lowermost right fold segment does not topographically express with fluvial erosion. Folding velocity is higher at the final

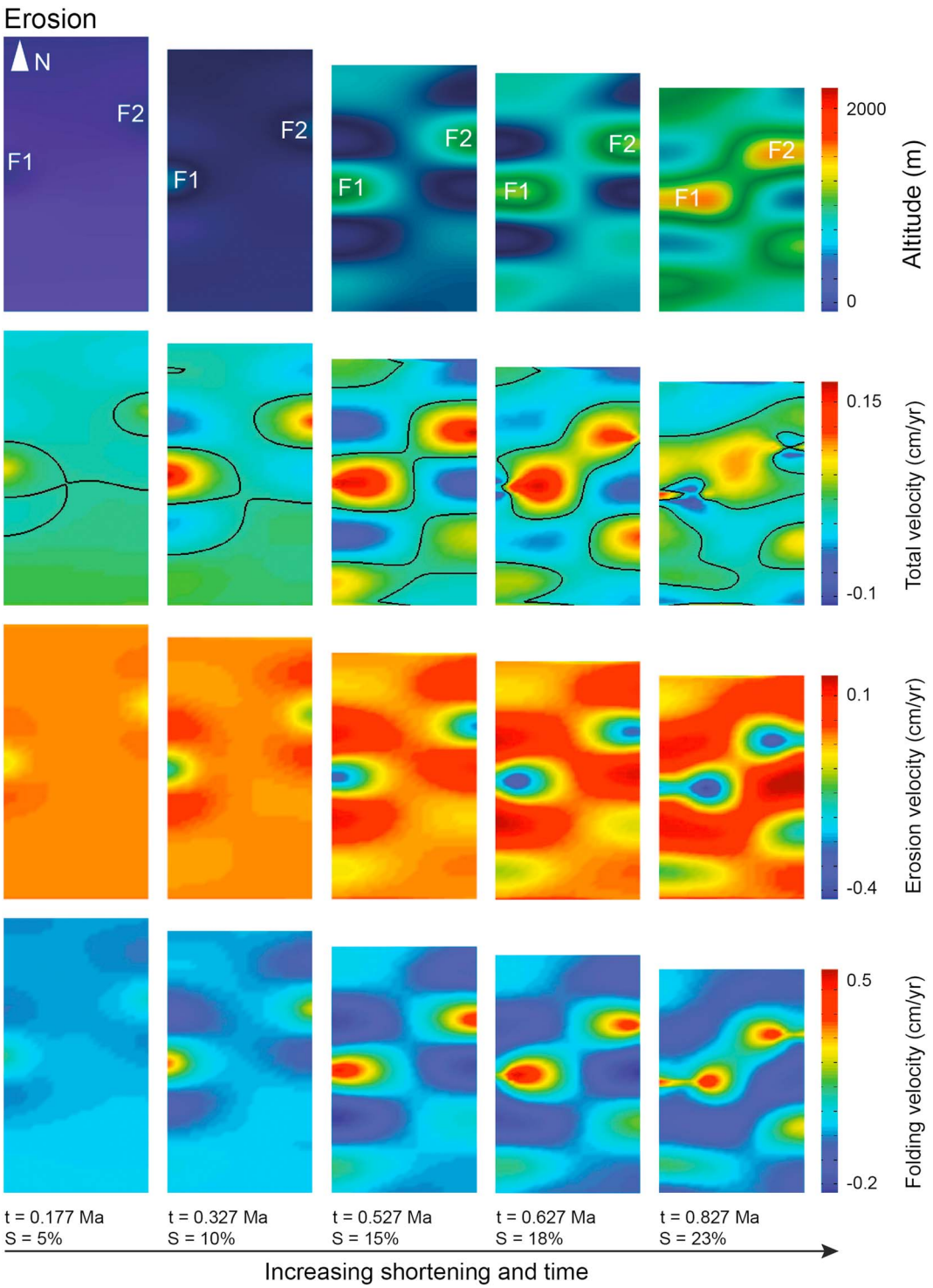

Figure 9. Evolution of topography and velocities through time for the case with linear diffusion erosion ($c = 0$, $k = 8 \times 10^{-7}$ m^2 s^{-1}). Total velocity = sum of the folding and erosion velocities. The black contour line at 0. Initial regional slope $\beta = 0.5$ % and initial distance $D = 8$ km.

stage of the simulation (38%) than in the case without fluvial erosion (Figure 7). Linkage between fold segments can be predicted by looking at the folding velocity pattern and its magnitude. For example, at 23% shortening folding velocity of F2 already started to decrease and is lower than the folding velocity of the segment south of F2, when no erosion is present. In contrast, folding velocities of F1 and F2 are still high

when fluvial erosion is considered (Figure 7). The velocity of the fold segment south of F2 is similar to those of F1 and F2. At 28%, it is clear that F1 will link with the fold segment south of F2 if no fluvial incision occurs. If fluvial erosion is considered, it is unclear with which fold segment F2 will link. Increasing shortening further (38%) enhances the chance that F2 will link with the segment north of F1. Erosion tends to modify the relative growth of fold segments (with respect to each other), which results in different interactions and linkage modes than when no fluvial erosion is present. The fact that folding velocity remains larger in the case with erosion compared to the case without erosion suggests that erosion enhances folding.

3.3.2. Hillslope Processes (Linear Diffusion)

In a next set of simulations, we simplified the surface processes to only one parameter, setting the fluvial incision to zero ($c = 0$) to quantify the relation between erosion and folding growth rate. Erosion and deposition of sediments are here modeled as a linear diffusive process [*Culling*, 1960]. We considered the same initial conditions (i.e., $D = 7.5$, 8, or 8.5 km and $\beta = 0.5$ %) as before but used different values of diffusivity, k ($4 \times 10^{-7}\,m^2\,s^{-1}$ and $8 \times 10^{-7}\,m^2\,s^{-1}$). The presence of an initial regional slope increases the efficiency of the topography diffusion. According to the diffusion equation, one can predict the erosion velocity from the topography knowing:

$$V_{\text{erosion}} = \frac{\partial h}{\partial t} = K\left(\frac{\partial^2 h}{\partial x^2} + \frac{\partial^2 h}{\partial y^2}\right). \tag{2}$$

We present the evolution of topography, folding, erosion, and total velocities with increasing bulk shortening, for the case without (Figure 8, no hillslope processes) and with erosion and redeposition of sediments (hillslope processes, Figure 9). Negative values of the erosion velocity indicate erosion, while positive values are related to the deposition of sediments. The total velocity is defined as the sum of the diffusive erosion and folding velocities. The folding velocity pattern corresponds to the topographic fold expression (Figure 8) when there is no erosion. The maximum folding velocities are first located at F1 and F2 and shift progressively to the adjacent fold segments in the north and south, with increasing shortening. The folding velocity is maximal at approximately 0.5 Ma and 15% shortening before it starts to decrease. At 23% shortening F1 and F2 do not and will not link. Instead, F1 links with the fold segment south of F2. Both the folding topography and folding velocity pattern are strongly modified by erosion (Figure 9). F1 and F2 link, but the other adjacent segments in the south and north of the model domain barely grow. The maximum folding velocity remains located at F1 and F2 (Figure 9), which may explain why the adjacent segments do not form clear topographic highs (Figure 9). The total velocity pattern in the case with erosion differs from the pattern without erosion (Figures 8 and 9). However, these variances are only visible after approximately 0.5–0.6 Ma and 15–18% and after the peak of folding velocity (Figure 9). They occur when the total velocity is lower than or equal to zero on the side of perturbations (black contour line in Figure 9). In other words, changes in the folding and total velocity patterns occur when the erosion velocity becomes larger than the folding velocity. After 15% shortening, the maximum total velocity, initially located at F1 and F2, moves laterally toward the center of the model. Positive values of the total velocity indicate that folding dominates over erosion such that topography is still developing. The folding velocity pattern follows a similar temporal evolution. Maximum folding velocities, initially located at F1 and F2, shift toward the center of the model, pinch out, and thin toward the sides of the model. The locations with fastest erosion coincide with the highest topography and maximum folding velocities, at the location of F1 and F2. After 23% shortening, F1 links with F2 if erosion is present, and their wavelength is larger than without erosion.

We computed the evolution of maximum amplitude, folding, and erosion velocities (Figure 10) for a vertical section (section *AA*′, Figure 10) in the direction of compression (y direction), for cases without erosion, as well as with medium and high erosion rates (using medium, $4 \times 10^{-7}\,m^2\,s^{-1}$, and high, $8 \times 10^{-7}\,m^2\,s^{-1}$, values for diffusivity). Transect *AA*′ records the growth of the perturbation P1 in z (fold amplification) and y directions (sequential growth). While the topographic amplitude of the fold tends to decrease, the instantaneous folding velocity increases with increased erosional efficiency. This apparently contradictive observation suggests that erosion enhances exhumation of deeper material (hence high folding velocity) but erosion is too intense to allow fold amplification and growth of topography.

The folding velocity differs between cases with and without erosion. We observe for the case without erosion a first peak around 0.5 Ma, a progressive decrease of the velocity until 1.4 Ma, before a second increase

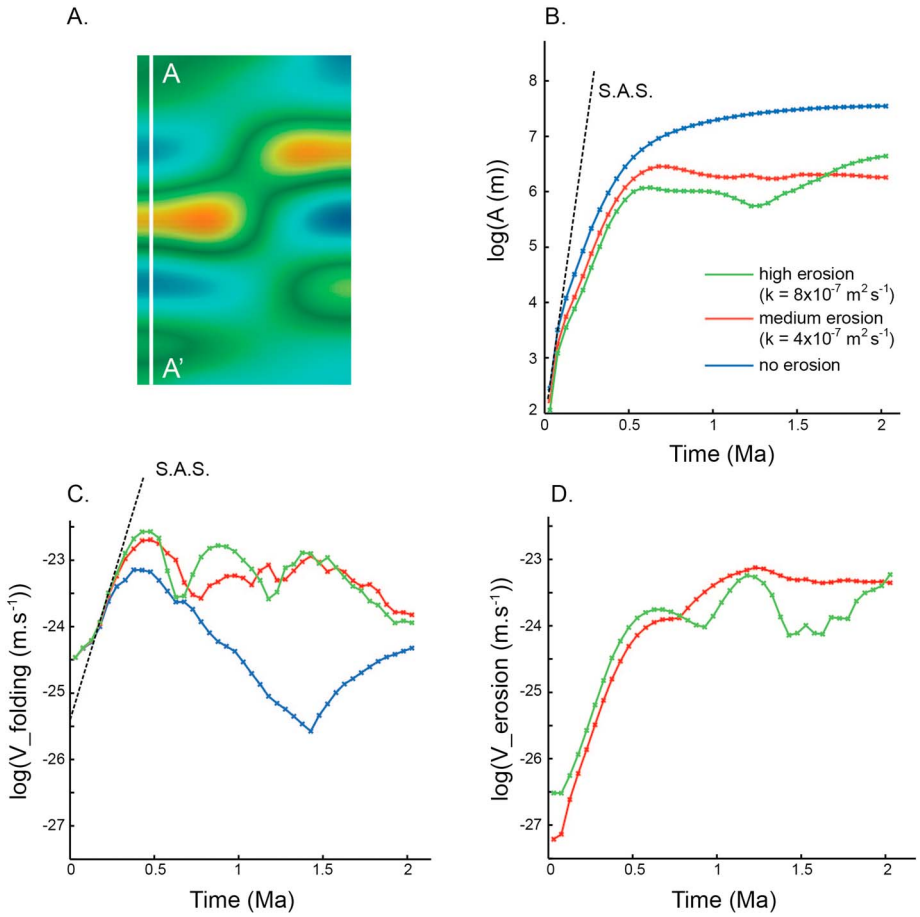

Figure 10. (a) Map view of the topography of one simulation after 23% of shortening. Line *AA'*: location of the vertical topographic section from which the curves in Figures 10b–10d were obtained. (b) Evolution of the amplitude, (c) evolution of the folding velocity, and (d) evolution of the erosion velocity for three different erosional regimes. An initial regional slope $\beta = 0.5$ %, a fluvial coefficient $c = 0$, and initial distance $D = 8$ km. S.A.S: small-amplitude solution, predicting an analytical solution for the initial exponential phase of growth fold [*Fletcher*, 1991, 1995].

(Figure 10). The first peak corresponds to the initial exponential amplification of P1 [*Fletcher*, 1991], while the decrease corresponds to the moment where fold growth is controlled by the arclength and shortening of the sediment layer [*Schmalholz and Podladchikov*, 2000]. *Schmalholz and Podladchikov* [2000] refer to this latter growth as the layer length-controlled growth. The second peak corresponds to the initial exponential amplification of an adjacent segment in the south (Figure 9), which forms due to the sequential growth of P1. The interpretation of the various peaks is slightly more difficult for the case with erosion. The maximum folding velocity remains at the location of F1 and F2 and does not migrate toward the adjacent segments (Figure 9). One can, however, deduce that the first peak corresponds to the amplification of P1 at approximately 0.53 Ma, by comparing the evolution of the folding pattern of Figure 9, and the transect *AA'* on Figure 10. The subsequent decrease at approximately 0.63 Ma (Figure 10) corresponds to the moment when elongation of F1 is enhanced and when the maximum folding velocity shifts laterally toward the center of the model (at 18% shortening, Figure 9). The second peak at 0.83 Ma (Figure 10) corresponds to the maximum folding velocity (Figure 9) of F1. The amplification of P1 is maintained by erosion. Maximum values of erosion and folding velocities are not in phase but present a slight shift in time. The maximum of erosion velocity occurs after the maximum of folding velocity, which is caused by the erosion time response to tectonic forcing.

According to the evolution of the folding velocity pattern in Figure 9, erosion enhances fold elongation at approximately 0.63 Ma. This occurs after the initial exponential growth phase, described by *Fletcher* [1991] (plotted as a dotted line in Figure 10). Erosion controls fold elongation, during the phase when fold growth is controlled by the shortening and arclength of the sediment layer [*Schmalholz and Podladchikov*, 2000].

Modeled erosion is a function of topography and requires that relief must be developed to be efficient and to have the possibility of influencing the ongoing deformation. Erosion increases as rapidly as the folding velocity during the first exponential amplification of the perturbation P1 (Figure 10). After this initial amplification phase, erosion velocity tends to stabilize, similarly to fold growth (Figures 10b and 10c). During the exponential phase amplification of the perturbation P1, topography developed quickly, which triggers erosion. During the subsequent layer length-controlled growth, erosion enhances amplification of P1 due to unloading of the fold segment F1. Thus, after the initial exponential fold growth, folding velocities remain significant (Figure 10c, red and green lines), instead of decreasing as expected from the finite amplitude solution [*Kaus and Schmalholz*, 2006; *Schmalholz and Podladchikov*, 2000] for a case without erosion (Figure 10c, blue line). The ratio between folding and erosion velocities controls if and when erosion can enhance fold elongation. Therefore, for high values of the diffusion coefficient, erosion velocity should be higher and the discussed effect should occur earlier (see equation (1)). However, if this coefficient is too high, then all topography is diffused and folds do not show any topographic expression at the surface.

4. Discussion

4.1. General Observation

Results indicate that while an initial regional slope tends to reduce the critical distance for the two perturbations to link, fluvial incision and/or hillslope diffusion increases this distance. Moreover, erosion and sedimentation strongly influence the velocity pattern and have the capacity to enhance fold elongation.

The initial regional slope introduces thickness variations in the sediment layer, which has the capacity to modify the fold growth rate. Increasing the thickness of the overburden results in an increase of lithostatic pressure. Consequently, folding preferentially occurs in the thinnest parts of the model where lithostatic pressure is lower. The overburden is less competent and requires less force to bend. The fold segments in the south will amplify and elongate faster than P2 and may link with P1, as they are now at shorter horizontal distances than P2. However, even if the regional slope affects the fold growth rate, the wavelength of F1 and F2 does not change. This may be explained by the fact that even though we are in a detachment folding mode, the parameters also indicate that we are close to a gravity-controlled mode, and that gravity would actually play a role.

Surface processes modify the folding pattern by affecting fold interactions. While erosion is enhancing the fold growth rate, redistribution of mass by hillslope processes increases the fold wavelength. These findings are in agreement with previous studies [*Goff et al*., 1996; *Simpson*, 2004c]. The critical distance D_{crit} is thus increased, due to the increase in wavelength of the fold segments.

However, the capacity of erosion and sedimentation to affect D_{crit} or to modify the folding patterns depends on the surface process model (i.e., linear or nonlinear diffusion law). The fold pattern is more similar to the one obtained without erosion and sedimentation, and the critical distance is smaller with the nonlinear diffusion model, accounting for both hillslope and fluvial processes than with the linear diffusion model. This is because erosion and sedimentation act at local scales in the nonlinear diffusion model and may localize the deformation. In the nonlinear diffusion model, intensity of fluvial incision is governed by the diffusion coefficient, which itself depends on the local slope and contributing area. Rivers developed first on the sides of the growing fold segments F1 and F2, where topography is the highest. Deformation can be localized at the river if river incision is sufficient enough and fold elongation can be slowed down or stopped. However, redistribution of mass in the model remains focused around topographic heighs, and thus, the folding velocity is only affected locally. Although erosion and sedimentation enhance fold growth rates, they do not affect the wavelength of the fold segments. This is due to the local redistribution of masses between growing fold segments and is related to the connectivity of the drainage network at large sale. Indeed, as discussed by *Simpson* [2004b], the capacity of surface processes to influence 3-D folding and modify fold wavelength is related to the length scale over which sediment transport takes place and is greatly dependent on the temporal persistence of transverse drainage and a large-scale connectivity of the drainage network. In our models, however, the drainage network becomes quickly disconnected by the growth of fold segments, reorganized, and remains located at small basins in between fold segments. Consequently, erosion and sedimentation do not have the possibility to modify the fold pattern, and their effects remain mainly

located on the sides of the growing fold segments. In our model, rivers cannot then favor the development of double-plunging anticlines as suggested by *Simpson* [2004a]. However, previous numerical studies [*Fernandez and Kaus*, 2014; *Schmid et al*., 2008] have shown that these anticlines could also develop naturally, in the absence of erosion and sedimentation. To ensure long-range sediment transport, and to be able to see the potential influence on the fold patterns, the initial geometry and boundary conditions of the model should be modified. A setup similar to *Ruh et al*. [2013] where the bottom sheet is pulled out below a rigid backstop, such as in analogue modeling [*Konstantinovskaia and Malavieille*, 2005], would be more appropriate to address this. With such a configuration, folds develop in sequence with the deformation front moving away from the rigid backstop.

Distribution of mass is uniform over the entire model domain in the linear diffusion model. The folding velocity and fold pattern are then homogenously modified and not only at local scale, as it was in the nonlinear diffusion model. The wavelength of F1 and F2 is larger than with the nonlinear model, and F1 and F2 can link at larger initial distances D. However, D_{crit} must be limited in space, if one wants to use realistic values for the diffusion coefficient. Indeed, folds will not show any topographic expression, or fold amplification remains too low if extremely high diffusion coefficients are employed. Following *Grasemann and Schmalholz* [2012], an increase of the fold wavelength will result in a decrease of the ratio D/L and thus allows the fold segments to link at larger offsets D (Figure A2).

4.2. Comparison to Previous Studies

4.2.1. Numerical Modeling of Fold Linkage

Grasemann and Schmalholz [2012] investigated different linkage modes proposed in earlier theoretical models [*Bretis et al*., 2011; *Keller et al*., 1999; *Ramsey et al*., 2008]. They proposed four types of fold interactions and introduced two dimensionless ratios to quantify the transition from linkage to no linkage. The first is the ratio of the offset D to the low limb-dip wavelength developing in the numerical simulation L [*Grasemann and Schmalholz*, 2012, Figure 2]. The second is the ratio of the amplitude in the horizontal middle of the plate (A_{mid}) to the maximal amplitude (A_{max}; see Figure 3). *Grasemann and Schmalholz* [2012] considered that the transition from linkage to no linkage mode occurs when A_{mid}/A_{max} becomes negative and for values of D/L between 0.6 and 0.8 depending on the chosen rheological law (i.e., linear viscous or power law).

Our results are similar to those of *Grasemann and Schmalholz* [2012]. We also obtained a transition from linkage to no linkage modes for $D/L = 0.6$ and a change of sign of the ratio A_{mid}/A_{max} (Figure 3). However, we obtained only three of the four linkage modes: linear linkage (for $D = 0$ km), oblique linkage ($0 < D < 8$ km), and oblique no linkage ($D > 8$ km). The linear no linkage mode was not reproduced in our models. Instead, we additionally obtained a case where fold segments are locked. This can be explained by the initial and boundary conditions of our model. Although the dimensions of our model are similar to those of *Grasemann and Schmalholz* [2012], the viscosity contrast and the thickness ratio of the stiff to weak layer are quite different. The growth rate and the dominant wavelength are consequently higher with the parameters we chose [*Fletcher*, 1991, 1995; *Schmalholz et al*., 2002]. In addition, contrary to *Grasemann and Schmalholz* [2012], our model is not symmetrical, as one of the perturbations is fixed in the middle of the model and the other is moved along the y axis. Consequently, the highest possible offset that can be investigated is slightly smaller than half of the initial length of the model (in y direction). The largest possible offset in our simulations is 20 km. The dominant wavelength of the perturbation being 13.2 km, it is likely that 20 km is insufficient to generate the linear no linkage mode.

The parameters used in our study (viscosity, thickness, density of the sediment, and décollement layers) fulfill all conditions for both detachment folding and gravity-controlled folding [*Schmalholz et al*., 2002], suggesting that folding should take place in the detachment folding mode but that gravity cannot be neglected. According to the parameters used in their study, the authors assumed that folding occurred in a detachment folding mode and that gravity was negligible. The locking mode observed in our simulations is not seen in the work of *Grasemann and Schmalholz* [2012] but has been described in analogue models [*Dubey and Cobbold*, 1977].

Redistribution of mass due to erosion and redeposition of sediments (i.e., unloading of anticlines and loading of synclines) amplifies folding by gravity [*Burg et al*., 2004; *Simpson*, 2004c] and can thus affect the fold linkage modes proposed by *Grasemann and Schmalholz* [2012].

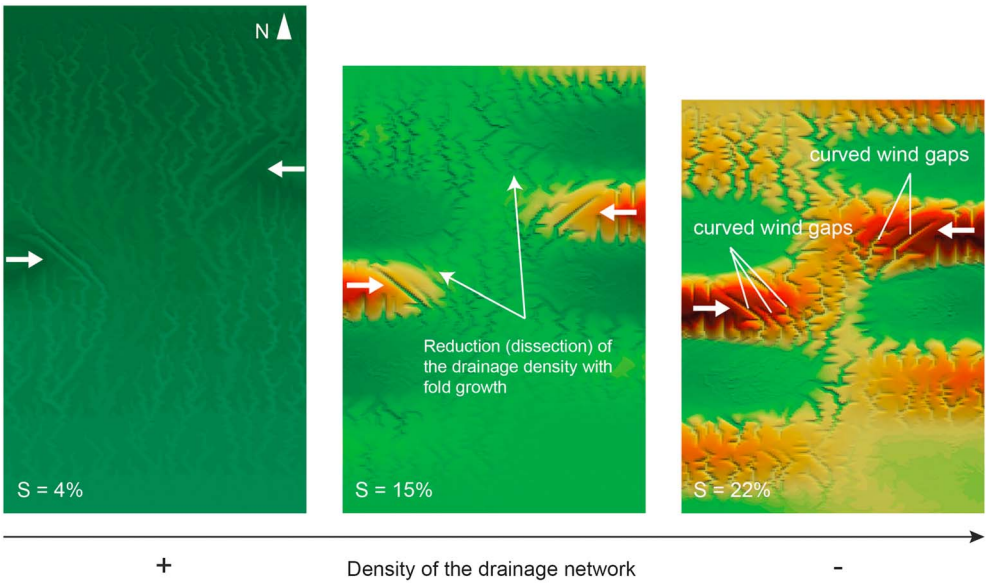

Figure 11. Evolution of the drainage network with increasing bulk shortening. White arrows: direction of growth of the initial prescribed perturbations (i.e., P1 and P2). Initial slope 0.5%, $D = 7$ km, and fluvial incision coefficient, $c = 100$.

Other numerical studies [*Fernandez and Kaus*, 2014; *Schmid et al*., 2008] investigated the evolution of fold patterns where the perturbations were randomly distributed and where multilayer systems were subjected to various loading conditions. The folds that develop in these models show all the lateral fold linkage modes investigated here and by *Grasemann and Schmalholz* [2012] for two isolated perturbations. Previous numerical studies [*Fernandez and Kaus*, 2014; *Schmid et al*., 2008] have reported triple linkage (i.e., lateral linkage of one fold with two other segments), which resembles some of our experiments, where fold segments seemed locked and it was unsure with which other fold segments they will link.

4.2.2. Geomorphic Studies

Many studies have used geomorphic observations to reveal and quantify tectonic activity; few have focused on fold elongation [*Bretis et al*., 2011; *Keller et al*., 1999; *Ramsey et al*., 2008]. *Keller et al*. [1999] identified six criteria to evaluate rates and directions of growth of active folds, namely, (1) decrease in drainage density and degree of dissection, (2) decrease in elevation of wind gaps, (3) decrease in relief of the topographic profile along the crest, (4) development of characteristic drainage pattern, (5) deformation of progressively younger deposits or landforms, and (6) decrease in rotation and inclination of forelimb. These criteria are consistent with fold elongation but do not prove it.

In our simulations, we were able to reproduce at least three of the criteria described by *Keller et al*. [1999]. As the drainage network reorganized during the growth of perturbations P1 and P2, several successive curved wind gaps (dry valleys for which a stream was deflected during fold growth) at the tips of F1 and F2 formed during increased bulk shortening (Figures 11 and 12a). The topographic profiles along the fold axis of F1 and F2 (profiles *AA*′ and *BB*′, Figure 12b) show a decrease in relief and in elevation of the successive wind gaps from the fold crest to their tips. Both the density and the degree of dissection of the drainage network decrease with elongation of fold segments (Figure 11). These curved wind gaps were observed in all our simulations with fluvial incision, independent of the investigated values of the fluvial incision parameter, and reproduce some of the natural wind gaps observed in the Zagros [*Bretis et al*., 2011, Figure 8].

We also observe a rotation of the streams on the flanks of F1 and F2 (toward the south, Figure 11) that face toward the direction of the regional slope. However, mainly due to the presence of the regional slope, we could not reproduce the well-developed fan-shaped tributary patterns that *Ramsey et al*. [2008] reported for the active folds of the Zagros Fold Belt. *Ramsey et al*. [2008] proposed that these tributaries formed during fold elongation. A possibility for which we did not generate these fan-shaped tributaries is the resolution of the SPM. Only high-order streams were resolved. To capture low-order streams, one should increase the resolution of the SPM. Resolution ratios between the surface process and mechanical codes

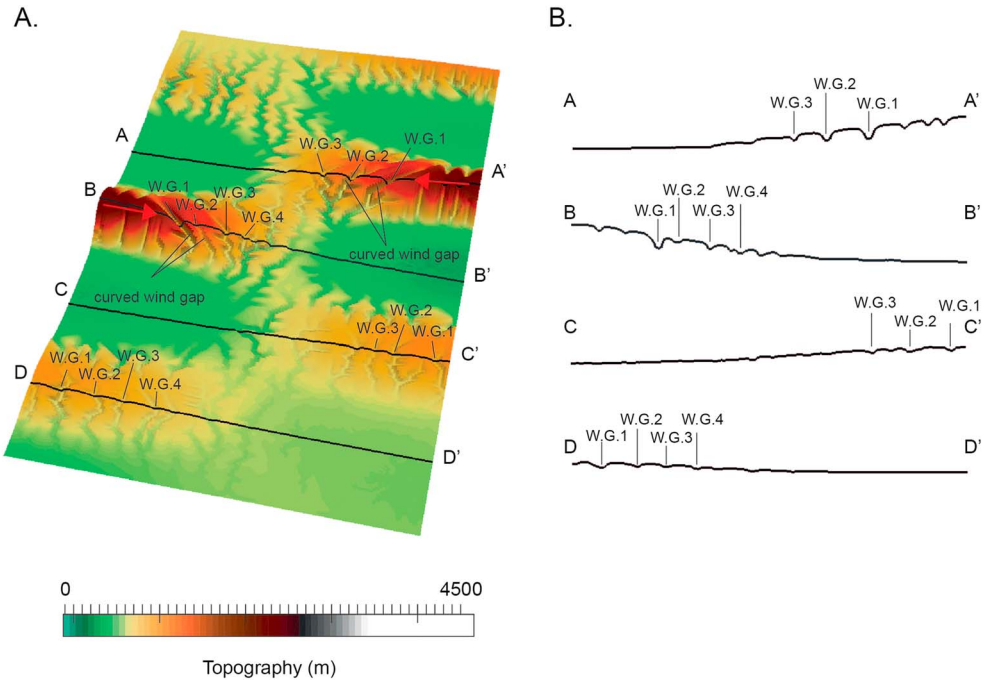

Figure 12. (a) Three-dimensional view of the surface topography of the model after a bulk shortening of 22% (see Figure 11 and caption for parameters). Red arrows: growth direction of perturbations. W.G.: wind gap. (b) Topographic profiles along the crests of the modeled folds. Lines *AA'*, *BB'*, *CC'*, and *DD'* are shown in Figure 12a.

were kept low (<10) to prevent numerical artifacts while simultaneously keeping the simulations computationally tractable.

The geomorphic criteria discussed in previous field studies [*Bretis et al.*, 2011; *Keller et al.*, 1999; *Ramsey et al.*, 2008] record the increase in topographic expression of folds with time. However, it might be difficult to conclude whether this topographic increase is due to the progressive exposure of a buried fold or the result of its elongation. However, in our work, we can observe that the drainage network results from fold elongation and several of the mentioned geomorphic indicators, such as the decrease in elevation of wind gaps, the decrease in density and degree of dissection of the drainage network, or the successive records of curved wind gaps, can be observed.

Drainage network is one of the most sensitive markers of deformation in tectonically active settings [*Burbank and Anderson*, 2001] and has been often used as a tool to provide indirect measurements of fold and fault kinematics. For example, long anticlines in the Zagros Fold Belt have been inferred from geomorphic markers to result from elongation and linkage of smaller fold segments. On the other hand, redistribution of mass (modeled with linear diffusion) has been recognized to affect fold amplification [*Contreras*, 2010; *Goff et al.*, 1996]. In this work, we also show that fluvial incision can affect the evolution of folding by enhancing fold growth rate and thus modify linkage between fold segments. If incision is sufficiently fast, fold elongation can be slowed or stopped. In that case, rivers do not only act as passive markers of ongoing deformation, as assumed by geomorphological studies.

4.3. Applications and Implications

4.3.1. Geological Applications

We focused on one particular tectonic feature: the fold linkage. We did not consider faulting and used a simple model without plasticity. Therefore, our simulations can only be applied to folds that form by buckling. The Zagros Fold Belt (ZFB) is a natural example where most of the shortening is accommodated by buckling with evidence of fold elongation and fold linkage [*Bretis et al.*, 2011; *Ramsey et al.*, 2008]. Although the thickness ratio between the salt layer and the sedimentary cover is not equivalent to that of the ZFB, the wavelength of the folds that developed in our simulations is close to that reported in the ZFB [*Mouthereau et al.*, 2006].

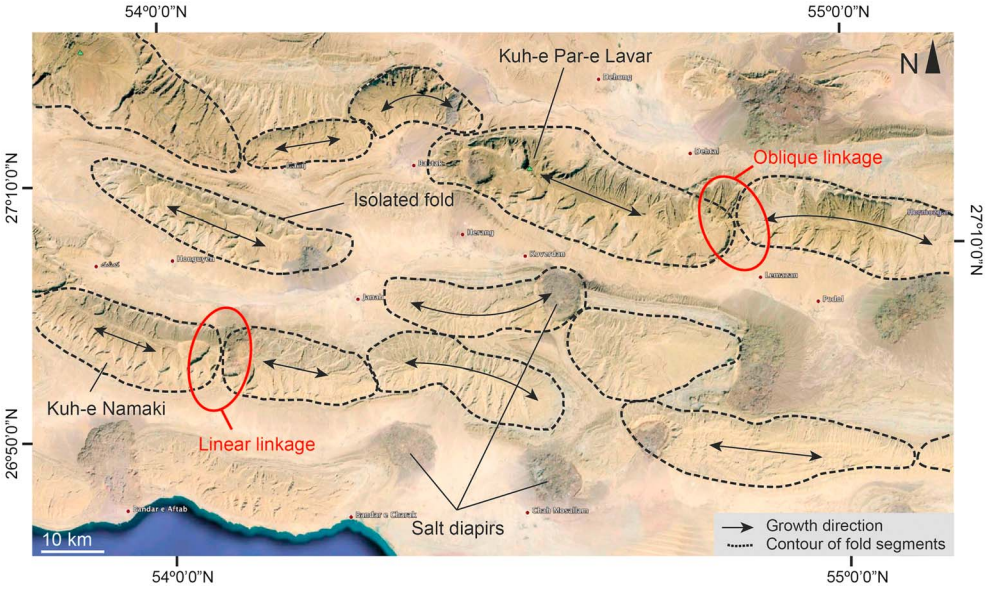

Figure 13. Plan view satellite image (Google Earth) of the Zagros Fold Belt, Fars Province, Iran. Dashed lines: outlines of fold segments with different fold linkage modes.

The distances observed at the end of the simulation (≈28% shortening) between fold segments F1 and F2 are in the range of those observed nowadays between fold segments in the ZFB (Figure 13). Diffusion rates, k, for surface processes are generally in the range of 100–5000 $m^2\,yr^{-1}$ for foreland depositional systems [*Flemings and Jordan*, 1989; *Goff et al*., 1996]. The values we used are between 30 and 300 $m^2\,yr^{-1}$ (i.e., approximately 10^{-7}–10^{-6} $m^2\,s^{-1}$). However, the erosion rates in the Zagros Mountains are unknown, but supposedly low, according to present-day precipitations rates and climate [*Masoodian*, 2008], which are assumed to show little variations over the past million years [*Khadivi et al*., 2012]. Few cosmogenic studies were made due to the nature of the lithology (mainly carbonates), and the results are often difficult to interpret and even show some discordance [*Oveisi et al*., 2009]. Thus, we can assume that the parameters used in our models are consistent with the data from the ZFB.

Examples of fold linkage can be found in the Zagros fold-and-thrust belt of the Fars Province, Iran. The Kuh-e Namaki anticline is attributed to linear linkage, whereas the Kuh-e Par-e Lavar is attributed to oblique linkage (Figure 13). Similarly, in the Kurdistan region of Iraq, *Bretis et al*. [2011] suggested that the Quara Chauq and Safeen anticlines formed by oblique linkage, whereas the Kirkuk anticline results from linear linkage. The ocking case can be compared to some case in the ZFB where small segments are isolated between two long train anticlines (Figure 13). The collision-related deformation on the Arabian continental margin has been recorded in middle Miocene times [*Mouthereau et al*., 2006]. This, and the analysis of present-day topography, tend to suggest that an initial topographic slope was present before the recent growth of fold (probably less than 3 Ma) [*Mouthereau et al*., 2012]. According to our simulations, fold linkage is only modified under moderate to high erosion ($k \approx 3000\,m^2\,yr^{-1}$). It is most likely that fold linkage in the Fars Province has been affected by the presence of an initial topographic slope rather than by surface processes. However, changing the viscosity contrast and strain rate, and thus modifying the fold growth rate, can affect the fold linkage at lower erosional regimes ($k < 3000\,m^2\,yr^{-1}$).

4.3.2. Economic Implications

Fold-and-thrust belts are of economic interest and contain 14% of the known and 15% of the undiscovered global recoverable hydrocarbons [*Bretis et al*., 2011; *Cooper*, 2007]. The Zagros, in particular, is one of the largest fold-and-thrust belts with hydrocarbons [e.g., *Colman-Sadd*, 1978; *Lacombe et al*., 2007; *Mouthereau et al*., 2012; *Vergés et al*., 2011]. The hydrocarbon traps in the Zagros Fold Belt are mainly associated with antiformal structures. Hence, it is of economic interest to understand the evolution of folds and how they link together, as this determines the connectivity between reservoirs. One critical aspect is the saddle point that can control the migration of hydrocarbon within the reservoir. In this work, we did not consider faulting and thus connectivity between

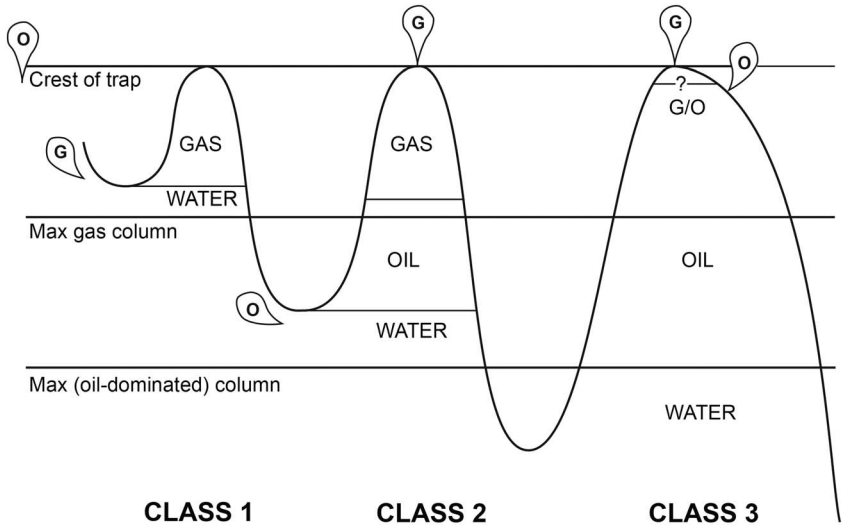

Figure 14. Schematic representation of the different hydrocarbon traps and their characteristic fill. Bubbles (G: gas and O: oil) are type of fluid spilled or leaked. G/O: gas-oil contact (redrawn from *Sales* [1997]).

reservoirs is controlled by fold linkage. However, in nature reservoirs can also be connected through faults. In an antiformal trap (e.g., fold), the closure is defined as the vertical distance between the saddle point (or spill point) and the crest of the anticline (or top of the trap). The seal strength corresponds to the height of the hydrocarbon column that the seal can retain before to start leaking. In hydrocarbon traps, the ratio of closure to seal strength controls what is retained, leak, and/or spill. Three classes of traps have been defined [*Sales*, 1997] using two key hydrocarbon columns, as threshold and their relative position to spill points (Figure 14). These two columns are the maximum gas column and the highest possible oil-dominated column. The distribution of hydrocarbons, as well as the migration mode (i.e., spilling versus leaking), is different for each class. While spilling refers to bed-parallel flow at the base of the traps, leaking corresponds to flow through the seal (cap rock) that starts to fail by development of microstructures. While class 1 traps have excess seal strength, class 3 traps in contrary show a deficiency of seal strength relative to closure. Class 2 traps are intermediate. Class 1 traps contain gas, spill gas and oil, but leak neither. Class 2 traps contain both gas and oil, spill oil, and leak gas. Class 3 traps contain mainly oil, leak oil and gas, but spill neither [*Sales*, 1997].

In our simulations, the difference in elevation between the fold crests and the saddle point (i.e., the closure) increases with increased distance between two linking perturbations. Moreover, a steeper regional slope can modify the closure (Figures 4, 7, and 8), as well as the location of the saddle point. Although the influence of surface processes might be limited to the interactions between fold segments at the surface, the effect of the regional slope can affect the amplification of folds at deeper stratigraphic levels and thus modify the class of hydrocarbon trap. Therefore, if the closure increases, without modifying the seal strength, the trap can contain more oil. The extent to which the fold interactions observed at surface in the present study can be extrapolated to the saddle point at depth should be further studied, but the potential influence of trap formation cannot be neglected. Furthermore, the relation between fold amplification and thickness of the overburden or detachment can be used to infer the closure of a trap in antiformal reservoirs. As folds amplify higher in the parts of the model where the overburden is smaller, one can expect a higher closure of the traps. Similarly, if traps have high closure, we could expect either a variation in thickness of the overburden or a thicker detachment.

5. Conclusions

We investigated the effect of surface processes and/or the presence of an initial surface slope on fold linkage. Both erosion and redeposition of sediments enhance elongation of folds and allow linkage of initially spaced perturbations. Elongation is enhanced by erosion and sedimentation when the erosion velocity becomes larger than fold amplification. Fold elongation only occurs after the exponential amplification phase of the fold. An initial regional slope introduces thickness variations in the overburden that reduce the critical distance D_{crit}. In contrast, erosion, and sedimentation increase D_{crit} and allow fold segments initially located

at larger distances to link. The location of the saddle point, as well as its vertical distance to the crest of anticlines, can also be strongly modified. This distance characterizes the closure of a hydrocarbon trap and is of great economic interest as it can influence the nature and migration of hydrocarbons. With the parameters used by our model, the results can be applied to the Zagros Fold Belt, where several cases of fold elongation and fold linkage have been documented.

Appendix A

The mathematical model employed in this study consists of a fully coupled 3-D mechanical and surface processes model. By fully coupled, we refer here to the coupling between the surface processes and mechanical models, and not to fully coupled thermomechanical model, as we here do not consider any temperature gradient for the deformation. Fully coupled implies a full feedback between the codes and that both codes can influence each other. The model is described in details in *Collignon et al*. [2014].

A1. Mechanical Model

The model solves the equations describing the conservation of momentum and mass for a highly viscous, incompressible fluid. Using the relationship between the total (σ_{ij}) and deviatoric $\left(\sigma'_{ij}\right)$ stress tensor, the conservation of momentum for highly viscous flow (i.e., Stokes equation of slow flow) can be written as

$$\frac{\partial \sigma'_{ij}}{\partial x_j} - \frac{\partial P}{\partial x_i} + \rho g_i = 0, \tag{A1}$$

where i and j refer to the three spatial coordinates x,y, and z, respectively; g_i is the ith component of the gravity vector $\vec{g} = \left(g_x, g_y, g_z\right)$. $P = -\frac{1}{3}\left(\sigma_{xx} + \sigma_{yy} + \sigma_{zz}\right)$, is the total pressure and ρ the density. Stresses and the pressure are related via $\sigma_{ij} = \sigma'_{ij} - P\delta_{ij}$, where δ_{ij} is the Kronecker delta.

The conservation of mass, assuming incompressibility, is given by

$$\frac{\partial v_i}{\partial x_i} = 0. \tag{A2}$$

In this work we consider linear viscous materials with the following constitutive relationship:

$$\sigma'_{ij} = 2\eta\dot{\varepsilon}_{ij}, \tag{A3}$$

where

$$\dot{\varepsilon}_{ij} = \frac{1}{2}\left(\frac{\partial v_i}{\partial x_j} + \frac{\partial v_j}{\partial x_i}\right), \tag{A4}$$

is the strain rate tensor and η is the shear viscosity.

A2. Surface Processes Model

Erosion and deposition of sediments have the capacity to influence the deforming model by modifying the distribution of vertical surface load and by changing the thickness of the upper layer. The surface processes model considers transport-limited conditions and take into account both fluvial incision and hillslope diffusion. We follow the formulation of *Simpson and Schlunegger* [2003], in which the surface processes model is governed by a system of two equations with two unknown functions, the topography $h(x,y,t)$ and the surface water discharge $q(x,y,t)$. The system of equation describing the evolution of topography is given by

$$\frac{\partial h}{\partial t} = \nabla \cdot \left((c\boldsymbol{q}^m + k)\nabla h\right), \tag{A5}$$

$$\nabla \cdot \left(\frac{\nabla h}{|\nabla h|}\boldsymbol{q}\right) = -\alpha, \tag{A6}$$

where k is the hillslope coefficient, c the fluvial incision, α the precipitation rates (in excess of infiltration), and m a fluvial incision power exponent. This model uses a simple formulation and thus neglects certain aspects

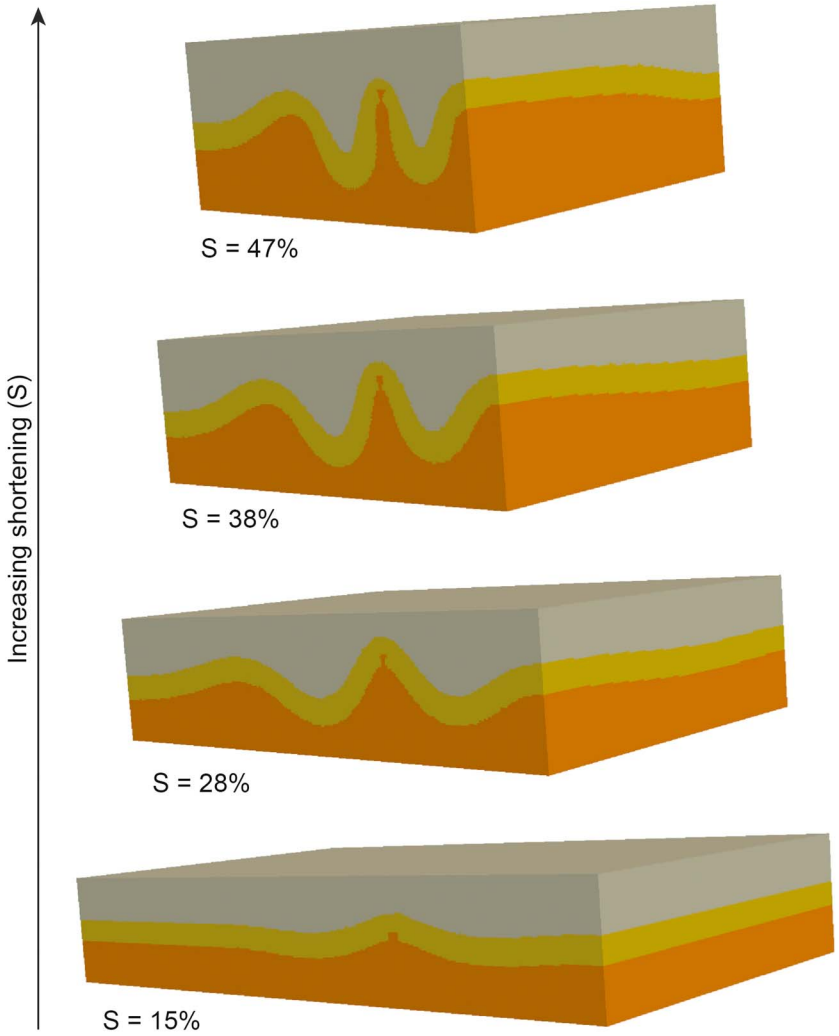

Figure A1. Three-dimensional evolution of the model shown in Figure 2, with increasing shortening. In this evolution we consider an offset of $D = 7.5\%$. No surface processes or initial topographic slope are present.

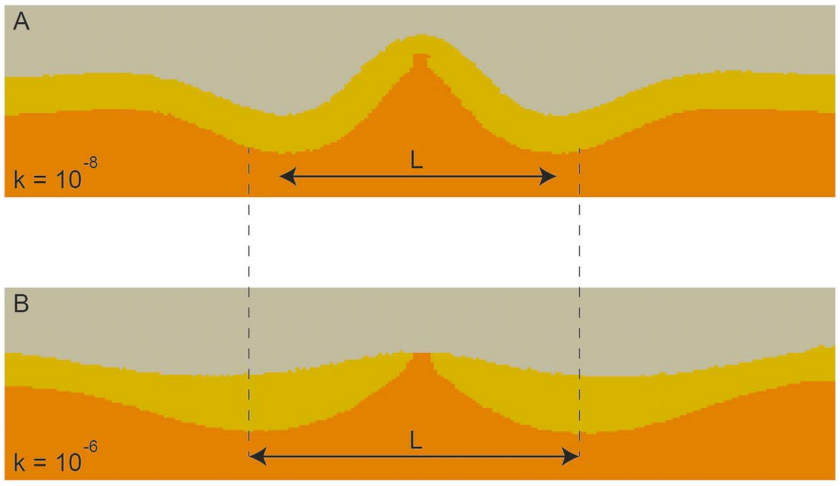

Figure A2. Model profile taken after 28% of shortening for different erosional regimes: (a) moderate diffusion rates (k in $m^2 s^{-1}$) and (b) intensive to extreme diffusion rates. L represents the wavelength of the fold. No initial topographic slope was present in both models.

such as landslides or detachment-limited conditions, which can have a great influence on the morphologic evolution of landscapes [*Tucker and Whipple*, 2002, and references therein].

A3. Three-Dimensional Model Evolution

Figure A1 shows the 3-D evolution of the model for a case without surface processes and without slope. This allows to also see the vertical evolution, as all the other figures represent map views, and shows that the entire model thicken, as well as the relative positions of the layers with respect to the top boundary.

A4. Effects of Erosion on Fold Wavelength

Figure A2 shows a vertical profile of models with different erosional conditions. The profiles clearly show that the wavelength becomes larger with increasing erosion and redistribution of sediments.

Acknowledgments
M. Collignon was funded by the European Union FP7 Marie Curie ITN "TOPOMOD" contract 26517. B. Kaus and N. Fernandez were funded by the ERC Starting grant 258830. Jonas Ruh, Leonardo Cruz, and Georges Hilley are thanked for their helpful and constructive review. The data for this paper are available by contacting the corresponding author at marine.collignon@erdw.ethz.ch.

References

Abbassi, M. R., and N. S. Mancktelow (1992), Single layer buckle folding in non-linear materials: I. Experimental study of fold development from an isolated initial perturbation, *J. Struct. Geol.*, *14*(1), 85–104.
Beaumont, C., P. Fullsack, and J. Hamilton (1992), Erosional control of active compressional orogens, in *Thrust Tectonics*, edited by K. R. McClay, pp. 1–18, Chapman, Hall, London.
Biot, M. A. (1961), Theory of folding of stratified viscoelastic media and its applications in tectonics and orogenesis, *Geol. Soc. Am. Bull.*, *72*, 1595–1620.
Biot, M. A. (1965), Theory of similar folding of the first and second kind, *Geol. Soc. Am. Bull.*, *76*, 251–258.
Biot, M. A. (1966), Three-dimensional gravity instability derived from two-dimensional solutions, *Geophysics*, *31*, 153–166.
Bonnet, C., J. Malavieille, and J. Mosar (2007), Interactions between tectonics, erosion and sedimentation during the recent evolution of the Alpine orogen: Analogue modeling insights, *Tectonics*, *26*, 1–15, doi:10.1029/2006TC002048.
Bretis, B., N. Bartl, and B. Graseman (2011), Lateral fold growth and linkage in the Zagros fold and thrust belt (Kurdistan, NE Iraq), *Basin Res.*, *23*, 615–630, doi:10.1111/j.1365-2117.2011.00506.
Burbank, D. (2002), Rates of erosion and their implications for exhumation, *Mineral. Mag.*, *66*(1), 25–52.
Burbank, D. W., and R. S. Anderson (2001), *Tectonic Geomorphology*, 270 pp., Blackwell Scientific, Oxford, U. K.
Burg, J. P., and Y. Y. Podladchikov (1999), Lithospheric scale folding: Numerical modelling and application to the Himalayan syntaxes, *Int. J. Earth Sci.*, *88*, 190–200.
Burg, J. P., and Y. Podladchikov (2000), From buckling to asymmetric folding of the continental lithosphere: Numerical modelling and application to the Himalayan syntaxes, in *Tectonics of the Nanga Parbat Syntaxis and the Western Himalaya*, *Geol. Soc. Spec. Publ. London*, edited by M. A. Khan et al., pp. 219–236, Geol. Soc. London, London.
Burg, J. P., B. J. P. Kaus, and Y. Y. Podladchikov (2004), Dome structures in collision orogens: Mechanical investigation of the gravity/compression interplay, in *Gneiss Domes in Orogeny*, edited by D. L. Whitney, C. Teyssier, and C. S. Siddoway, pp. 47–66, Geol. Soc. Am. Spec. Pap., Boulder, Colo.
Cobbold, P. R. (1975), Fold propagation in single embedded layers, *Tectonophysics*, *27*, 333–351.
Collignon, M., B. J. P. Kaus, D. A. May, and N. Fernandez (2014), Influence of surface processes on fold growth during 3-D detachment folding, *Geochem. Geophys. Geosyst.*, *15*, 3281–3303, doi:10.1002/2014GC005450.
Colman-Sadd, S. P. (1978), Fold development in Zagros simply folded belt, southwest Iran, *Am. Assoc. Petrol. Geol. Bull.*, *62*, 984–1003.
Contreras, J. (2010), A model for low amplitude detachment folding and syntectonic stratigraphy based on the conservation of mass equation, *J. Struct. Geol.*, *32*, 566–579.
Cooper, M. (2007), Structural style and hydrocarbon prospectivity in fold and thrust belts: A global review, in *Deformation of the Continental Crust: The Legacy of Mike Coward*, *Geol. Soc. Spec. Publ. London*, edited by A. C. Ries, R. W. H. Butler, and R. H. Graham, pp. 447–472, Geol. Soc. London, London.
Crameri, F., H. Schmeling, G. J. Golabek, T. Duretz, R. Orendt, S. J. H. Buiter, D. A. May, B. Kaus, T. V. Gerya, and P. J. Tackley (2012), A comparison of numerical surface topography calculations in geodynamic modelling: An evaluation of the "sticky air" method, *Geophys. J. Int.*, *189*, 38–54.
Culling, W. E. H. (1960), Analytical theory of erosion, *J. Geol.*, *68*(3), 336–344.
Delcailleau, B., J.-M. Carozza, and E. Laville (2006), Recent fold growth and drainage development: The Janauri and Chandigarh anticlines in the Siwalik foothills, northwest India, *Geomorphology*, *76*, 241–256.
Dubey, A. K., and P. R. Cobbold (1977), Noncylindrical flexural slip folds in nature and experiment, *Tectonophysics*, *38*, 223–239.
Fernandez, N., and B. J. P. Kaus (2014), Fold interaction and wavelength selection in 3D models of multilayer detachment folding, *Tectonophysics*, *632*, 199–217.
Fillon, C., R. S. Huismans, and P. Van der Beek (2013), Syntectonic sedimentation effects on the growth of fold-and-thrust belts, *Geology*, *41*, 83–86.
Flemings, P. B., and T. E. Jordan (1989), A synthetic stratigraphic model of foreland basin development, *J. Geophys. Res.*, *94*, 3851–3866, doi:10.1029/JB094iB04p03851.
Fletcher, R. C. (1974), Wavelength selection in the folding of a single layer with power-law rheology, *Am. J. Sci.*, *274*, 1029–1043.
Fletcher, R. C. (1991), Three-dimensional folding of an embedded viscous layer in pure shear, *J. Struct. Geol.*, *13*(1), 87–96.
Fletcher, R. C. (1995), Three-dimensional folding and necking of a power-law layer: Are folds cylindrical, and, if so, do we understand why?, *Tectonophysics*, *247*, 65–83.
Frehner, M. (2014), 3D fold growth rates, *Terra Nova*, *26*, 417–424.
Ghosh, S. K., and H. Ramberg (1968), Buckling experiments on intersecting fold patterns, *Tectonophysics*, *5*, 89–105.
Goff, D. F., D. V. Wiltschko, and R. C. Fletcher (1996), Décollement folding as a mechanism for thrust-ramp spacing, *J. Geophys. Res.*, *101*, 11,341–11,352, doi:10.1029/96JB00172.
Grasemann, B., and S. M. Schmalholz (2012), Lateral fold growth and fold linkage, *Geology*, *40*, doi:10.1130/G33613.1.
Grujic, D. (1993), The initial influence of initial fold geometry on Type 1 and Type 2 interference patterns: An experimental approach, *J. Struct. Geol.*, *15*, 293–307.

Johns, M. K., and S. Mosher (1996), Physical models of regional fold superposition: The role of competence contrast, *J. Struct. Geol.*, *18*, 475–492.
Jolley, S. J., D. Barr, J. J. Walsh, and R. J. Knipe (2007), *Structurally Complex Reservoirs*, *Geological Society of London Special Publication*, Geol. Soc. London, London.
Kaus, B. J. P., and S. M. Schmalholz (2006), 3D finite amplitude folding: Implications for stress evolution during crustal and lithospheric deformation, *Geophys. Res. Lett.*, *33*, L14309, doi:10.1029/2006GL026341.
Kaus, B. J. P., C. Steedman, and T. W. Becker (2008), From passive continental margin to mountain belt: Insights from analytical and numerical models and application to Taiwan, *Phys. Earth Planet. Inter.*, *171*, 235–251.
Kaus, B. J. P., A. Popov, and D. A. May (2012), Recent progress in modelling 3D lithospheric deformation, paper presented at EGU Spring meeting, Vienna.
Keller, E. A., L. Gurrola, and T. E. Tierney (1999), Geomorphic criteria to determine direction of lateral propagation of reverse faulting and folding, *Geology*, *27*, 515–518.
Khadivi, S., F. Mouthereau, J. Barbarand, T. Adatte, and O. Lacombe (2012), Constraints on palaeodrainage evolution induced by uplift and exhumation on the southern flank of the Zagros-Iranian Plateau, *J. Geol. Soc. London*, *169*, 83–97.
Konstantinovskaia, E., and J. Malavieille (2005), Erosion and exhumation in accretionary orogens: Experimental and geological approaches, *Geochem. Geophys. Geosyst.*, *6*, Q02006, doi:10.1029/2004GC000794.
Lacombe, O., K. Amrouch, F. Mouthereau, and L. Dissez (2007), Calcite twinning constraints on late Neogene stress patterns and deformation mechanisms in the active Zagros collision belt, *Geol. Soc. Am.*, *35*, 263–266.
Mancktelow, N. S. (2001), Single-layer folds developed from initial random perturbations: The effects of probability distribution, fractal dimension, phase and amplitude, in *Tectonic Modeling: A Volume in Honor of Hans Ramberg*, edited by H. A. Koyi and N. S. Mancktelow, pp. 69–87, Geol. Soc. Am. Mem., Boulder, Colo.
Masoodian, S. A. (2008), On precipitation mapping in Iran, *J. Humanit. Univ. Isfahan*, *30*(2), 69–80.
Molnar, P., and P. England (1990), Late Cenozoic uplift of mountain ranges and global climate change: Chicken or egg?, *Nature*, *346*, 29–34.
Montgomery, D. R., and M. T. Brandon (2002), Topographic controls on erosion rates in tectonically active mountain ranges, *Earth Planet. Sci. Lett.*, *201*, 481–489.
Mouthereau, F., O. Lacombe, and B. Meyer (2006), The Zagros folded belt (Fars, Iran): Constraints from topography and critical wedge modelling, *Geophys. J. Int.*, *165*, 336–356.
Mouthereau, F., O. Lacombe, J. Tensi, N. Bellahsen, S. Kargar, and K. Amrouch (2007), Mechanical constraints on the development of the Zagros Folded Belt (Fars), in *Thrust Belts and Foreland Basins: From Kinematics to Hydrocarbon Systems—Frontiers in Earth Sciences*, edited by O. Lacombe, J. Roure, and J. Vergés, pp. 245–264, Springer, Berlin.
Mouthereau, F., O. Lacombe, and J. Vergés (2012), Building the Zagros collisional orogens: Timing, strain distribution and dynamics of Arabia/Eurasia plate convergence, *Tectonophysics*, *532-535*, 27–60.
Nalpas, T., I. Györfi, F. Guillocheau, F. Lafont, and P. Homewood (1999), Influence of sediment loading on growth folds. Analogue modelling and field study (southern border of the Jaca basin), *Bull. Soc. Geol. Fr.*, *170*(5), 733–740.
Nalpas, T., D. Gapais, J. Vergés, L. Barrier, V. Gestain, G. Leroux, D. Roubly, and J. J. Kermarrec (2003), Nature of synkinematic sedimentation on the growth of compressive structures constrained by analogue models and field examples, *Geol. Soc. London Spec. Publ.*, *208*, 307–319.
Oveisi, B., J. Lavé, P. Van der Beek, J. Carcaillet, L. Benedetti, and C. Aubourg (2009), Thick- and thin-skinned deformation rates in the central Zagros simple folded zone (Iran) indicated by displacement of geomorphic surfaces, *Geophys. J. Int.*, *176*, 627–654.
Pichot, T., and T. Nalpas (2009), Influence of synkinematic sedimentation in a thrust system with two decollement levels: Analogue modelling, *Tectonophysics*, *473*, 466–475.
Popov, A., and B. Kaus (2013), LaMEM (Lithosphere and Mantle Evolution Model): Advancing a staggered-grid finite difference version of the code, paper presented at EGU, Vienna.
Ramsey, L. A., R. T. Walker, and J. Jackson (2008), Fold evolution and drainage development in the Zagros mountains of Far provinces, SE Iran, *Basin Res.*, *20*, 23–48.
Ruh, J. B., T. V. Gerya, and J. P. Burg (2013), High-resolution 3D numerical modeling of thrust wedges: Influence of décollement strength on transfer zones, *Geochem. Geophys. Geosyst.*, *14*, 1131–1155, doi:10.1002/ggge.20085.
Sales, J. K. (1997), Seal strength vs. trap closure: A fundamental control on the distribution of oil and gas, in *Seals, Trap, and the Petroleum System*, edited by R. C. Surdam, pp. 57–83, AAPG Mem, Boulder, Colo.
Schmalholz, S. M. (2008), 3D numerical modeling of forward folding and reverse unfolding of a viscous single-layer: Implications for the formation of folds and fold pattern, *Tectonophysics*, *446*, 31–41.
Schmalholz, S. M., and Y. Podladchikov (2000), Finite amplitude folding: Transition from exponential to layer length controlled growth, *Earth Planet. Sci. Lett.*, *179*, 363–377.
Schmalholz, S. M., Y. Podladchikov, and J. P. Burg (2002), Control of folding by gravity and matrix thickness: Implications for large-scale folding, *J. Geophys. Res.*, *107*(B1), 2005, doi:10.1029/2001JB000355.
Schmid, D. W., and Y. Podladchikov (2006), Fold amplification rates and dominant wavelength selection in multilayer stacks, *Philos. Mag.*, *86*(21–22), 3409–3423.
Schmid, D. W., M. Dabrowski, and M. Krotkiewski (2008), Evolution of large amplitude 3D fold patterns: A FEM study, *Phys. Earth Planet. Int.*, *171*, 400–408.
Simpson, G. (2004a), Role of river incision in enhancing deformation, *Geology*, *32*, 341–344.
Simpson, G. (2004b), A dynamic model to investigate coupling between erosion, deposition, and three-dimensional (thin-plate) deformation, *J. Geophys. Res.*, *109*, F02006, doi:10.1029/2003JF000078.
Simpson, G. (2004c), Dynamic interactions between erosion, deposition, and three-dimensional deformation in compressional fold belt settings, *J. Geophys. Res.*, *109*, F03007, doi:10.1029/2003JF000111.
Simpson, G. (2006), Modelling interactions between fold-thrust belt deformation, foreland flexure and surface mass transport, *Basin Res.*, *18*, 125–143.
Simpson, G., and F. Schlunegger (2003), Topographic evolution and morphology of surfaces evolving in response to coupled fluvial and hillslope sediment transport, *J. Geophys. Res.*, *108*(B6), 2300, doi:10.1029/2002JB002162.
Tucker, G. E., and K. X. Whipple (2002), Topographic outcomes predicted by stream erosion models: Sensitivity analysis and intermodel comparison, *J. Geophys. Res.*, *107*(B9), 2179, doi:10.1029/2001JB000162.
Vergés, J. (2007), Drainage responses to oblique and lateral thrust ramps: A review, in *Sedimentary Processes, Environments and Basins: A Tribute to Peter Friend*, edited by G. Nichols, C. Paola, and E. A. Williams, pp. 29–47, Int. Assoc. Sediment.
Vergés, J., E. Saura, E. Casciello, M. Fernandez, A. Villasenor, I. Jimenez-Munt, and D. Garcia-Castellanos (2011), Crustal-scale cross-sections across the NW Zagros belt: Implications for the Arabian margin reconstruction, *Geol. Mag.*, *148*(5/6), 739–761.
Yamato, P., B. Kaus, F. Mouthereau, and S. Castelltort (2011), Dynamic constraints on the crustal-scale rheology of the Zagros Fold Belt, Iran, *Geology*, *39*, 814–818.
Zienkiewicz, O. C., and R. L. Taylor (2000), *The Finite Element Method. Vol. 1: The Basis*, Butterworth-Heinemann, Woburn.